Petroleum Science 23 (2026) 2367–2389

Contents lists available at ScienceDirect

Petroleum Science

journal homepage: www.keaipublishing.com/en/journals/petroleum-science

Original Paper

Adaptive weight strategy for frequency-decomposed seismic attribute fusion in predicting of complex sand body distributions

Hong-Li Wu [a,b], Sheng-He Wu [a,b,*], Zhen-Hua Xu [a,b], Ming-Cheng Liu [a,b], Bo Yang [a,b,c], De-Gang Wu [a,b], Zi-Shi Xie [a,b], Yu Tang [a,b], Xiao-Long Wan [a,b,d], Xin-Ping Zhou [d]

[a] National Key Laboratory of Petroleum Resources and Engineering, China University of Petroleum (Beijing), Beijing, 102249, China
[b] College of Geosciences, China University of Petroleum (Beijing), Beijing, 102249, China
[c] CNOOC Hainan Branch Company, Haikou, 570312, Hainan, China
[d] Research Institute of Exploration and Development, PetroChina Changqing Oilfield Company, Xi'an, 710018, Shaanxi, China

ARTICLE INFO

Article history:
Received 29 June 2025
Received in revised form
4 October 2025
Accepted 15 January 2026
Available online 20 January 2026

Edited by Xi Zhang and Jie Hao

Keywords:
Reservoir heterogeneity
Sand thickness prediction
Frequency-decomposed attribute
intelligent fusion
Adaptive weighting
Deep neural network

ABSTRACT

High-precision sand prediction is fundamental to improving the efficiency of oil and gas exploration and development. To address the limitations of traditional fixed-weight fusion strategies, particularly under conditions of significant lateral variation in sand body distribution, this study proposes a dynamic weighting–deep neural network (DW-DNN) for adaptive frequency-decomposed attribute fusion. The approach integrates physical constraints with deep learning and introduces two innovations: (i) a priori weight matrices derived from the amplitude–frequency and tuning thickness relationship (amplitude variation with frequency, AVF) are embedded into the attention mechanism to adaptively allocate multiband seismic attributes, emphasizing high-frequency features for thin sands and low-frequency features for thick sands; and (ii) a deep neural network with a composite loss function combining mean squared error (MSE) and AVF-based constraints is designed to jointly optimize weight allocation and prediction accuracy. The method was applied to the Xi 233 area of the Qingcheng Oilfield in the Ordos Basin and compared with conventional approaches. DW-DNN achieved high accuracy and generalizability, with an R^2 of 0.92 in the 30% blind-well test, 24.3% higher than conventional methods. In addition, 91% of well-point errors were within 0–3 m, while prediction accuracies for thin (≤3 m) and thick (>3 m) sands reached 88% and 91%, respectively. The model also maintained stable performance under low well-control conditions (training–test ratio 5:5). Predicted sand distributions exhibited improved continuity and geologically plausible geometries, clearly delineating channels, lobes, and estuary bars. The results demonstrate that DW-DNN enhances frequency-decomposed attribute fusion through adaptive weight allocation, providing a robust tool for predicting sand body distributions in complex reservoirs.

1. Introduction

As global oil and gas exploration increasingly emphasizes the investigation of deeper, unconventional, and structurally complex regions, the focus of reservoir target research has shifted from conventional reservoirs to more heterogeneous and intricate types. This transition presents significant challenges in the accurate prediction of sand body characteristics (Jia et al., 2023; Wang et al., 2025). Current methodologies for predicting sand body thickness predominantly fall into two main categories: statistical interpolation methods, which rely exclusively on well data, and integrated approaches, which amalgamate both well data and seismic data. The statistical interpolation method is effective in regions characterized by dense well coverage—specifically, where the interwell distance is less than the width of the sedimentary units (Ma et al., 2011; Saggaf and Nebrija, 2003). However, its accuracy experiences a pronounced decline in areas with sparse drilling, which is attributed to insufficient well density (Bitrus et al., 2016). Recent advancements in seismic data acquisition techniques and frequency decomposition technologies have

* Corresponding author.
E-mail address: reser@cup.edu.cn (S.-H. Wu).
Peer review under the responsibility of China University of Petroleum (Beijing).

https://doi.org/10.1016/j.petsci.2026.01.022

rendered frequency-decomposed seismic attribute fusion a promising strategy for reservoir prediction (Zhang et al., 2022).

The principle of seismic frequency-decomposed attribute fusion involves the analysis of seismic wave responses across various frequency bands in relation to the sand thickness. This methodological approach integrates multiple seismic attributes derived from diverse frequency bands through mathematical operations, thereby enhancing the interpretation of sand thickness (Chopra and Marfurt, 2005; Cui et al., 2024; Dorrington and Link, 2004; Li et al., 2024). Extensive research conducted by scholars has examined various frequency-decomposed attribute fusion techniques (Dong et al., 2024), which are generally categorized into linear and nonlinear methods on the basis of their fusion mechanisms (Fu et al., 2024; Sang et al., 2021; Wang et al., 2024; Yue et al., 2022; Zeng, 2017).

Linear fusion methods, which include color blending and multiple linear regression, utilize distinct techniques for seismic attribute integration (Yin et al., 2024). The color blending method maps seismic attributes onto color channels by employing color models such as RGB and HSV. This technique produces composite images through the superposition of colors, facilitating the rapid identification of sand distributions on the basis of parameters such as saturation or brightness (Li et al., 2019a, 2019b; Liu et al., 2024; Stark, 2006; Sun et al., 2024). A significant advantage of this methodology lies in its independence from drilling data; however, it primarily serves as a qualitative visualization tool and, consequently, does not fulfill the quantitative prediction objectives for sand bodies (Bitrus et al., 2016; Zeng, 2017; Zhang et al., 2025). Multiple linear regression is used to construct quantitative prediction models on the basis of linear assumptions, yielding reasonably accurate results when the distributions of the sand thickness are relatively uniform. Nonetheless, the efficacy of such linear models declines significantly in regions characterized by substantial spatial variations in sand thickness, where the relationship between seismic attributes and sand thickness assumes a nonlinear nature.

To address these challenges, nonlinear fusion methods have emerged, employing advanced machine learning algorithms designed to capture complex, nonlinear relationships between attributes and sand thickness. Prominent algorithms include support vector machines (SVMs), which handle high-dimensional nonlinear problems through the application of kernel mappings (Wang et al., 2013; Yin and Zhou, 2005). Genetic algorithms are also employed to optimize solutions via evolutionary strategies (Liu et al., 2024a). Neural networks, recognized for their ability to extract and reveal intricate feature relationships through multilayer nonlinear transformations, further contribute to this field (Ali et al., 2025; Xie et al., 2023; Zhen et al., 2024). Additionally, random forests utilize ensembles of decision trees to enhance predictive robustness, whereas ensemble learning methods integrate multiple predictive models to improve overall prediction stability (Liu et al., 2024b). Compared with their linear fusion counterparts, nonlinear algorithms have demonstrated superior accuracy in delineating complex thick sand boundaries.

Existing methodologies predominantly utilize a global fixed weight strategy, wherein a constant attribute weight coefficient is established through the comprehensive optimization of the training set. This approach, characterized by weight fixation, poses challenges in adapting to scenarios with substantial variations in the distribution of sand bodies within the layer (Gan et al., 2025; Xu et al., 2022). Consequently, there is an inability to dynamically integrate information across high- and low-frequency bands, ultimately hindering a thorough exploration of the response characteristics of seismic attributes linked to variations in sand thickness. These limitations restrict the prediction accuracy of the model. To address the issue of dynamic well-point weight allocation, the attention mechanism facilitates the capture of critical information through the dynamic allocation of feature weights, presenting a novel solution to this challenge (Bahdanau et al., 2014; Vaswani et al., 2017). Central to the fusion of seismic frequency-decomposed attributes is the establishment of an adaptable, nonlinear mapping relationship between frequency-decomposed attributes and the thickness of well-point sand. Given that shallow machine learning models possess constrained capabilities in resolving nonlinear complexities, deep learning methodologies have demonstrated promising predictive performance in recent years across the oil and gas sector (Chen et al., 2025), particularly in applications such as oil and gas production, lithology identification, and reservoir prediction (Liu et al., 2021; Niu et al., 2025; Yu et al., 2024; Zhao et al., 2023; Zhang et al., 2024). As the foundational architecture of deep learning, deep neural networks (DNN) have achieved remarkable advancements across various domains (Song et al., 2022; Zhang et al., 2022).

This paper presents a novel method for predicting sand bodies that integrates frequency-decomposed attributes with an adaptive weighting strategy known as the dynamic weight–based deep neural network (DW-DNN). The approach introduces an amplitude–frequency band, along with its relationship to the tuning thickness (amplitude variation with frequency, AVF), to establish a prior weight matrix. This matrix is further employed to guide the training process of the attention module. By incorporating the attention mechanism, which accounts for physical constraints, into the DNN model, the proposed method enhances the efficacy of frequency-decomposed attributes in the interpretation of sand bodies. Consequently, the model not only achieves improved accuracy but also enhances interpretability.

2. Methods and principles

The process of fusing frequency-decomposed seismic attributes involves three main steps (Fig. 1). First, seismic attributes from low, medium, and high-frequency bands are optimized (VÁCLAV, 2023). Next, well bypass attribute data are extracted from the frequency-decomposed seismic attributes. Finally, a nonlinear relationship between these seismic attributes and sand thickness is established via artificial intelligence methods, which enables the interpretation of sand characteristics on the basis of these attributes. However, when frequency-decomposed attributes are intelligently combined, the importance of seismic attributes in each frequency band for interpreting sand bodies can vary depending on their spatial position (Zhang et al., 2025). This variation arises from the rapid changes in the spatial distribution of the sand thickness. Therefore, assigning appropriate weights to seismic attributes across different frequency bands and spatial locations is essential. To address this challenge, this paper introduces a relationship between the AVF during the training process of the attention mechanism, which serves as a prior weight matrix. It also presents an adaptive weight allocation mechanism called the dynamic weight (DW), which functions under physical constraints. This mechanism is integrated into a DNN, resulting in a frequency-decomposed seismic attribute fusion method known as DW-DNN. This innovative approach employs an adaptive weight strategy to achieve high-precision predictions of sand bodies. This chapter explores ideas for improving DW-DNNs, the attention mechanism within physical constraints, and the deep neural network framework that incorporates these constraints.

2.1. Ideas for improvements

To allocate weights dynamically to seismic attributes within each frequency band during the process of frequency-decomposed

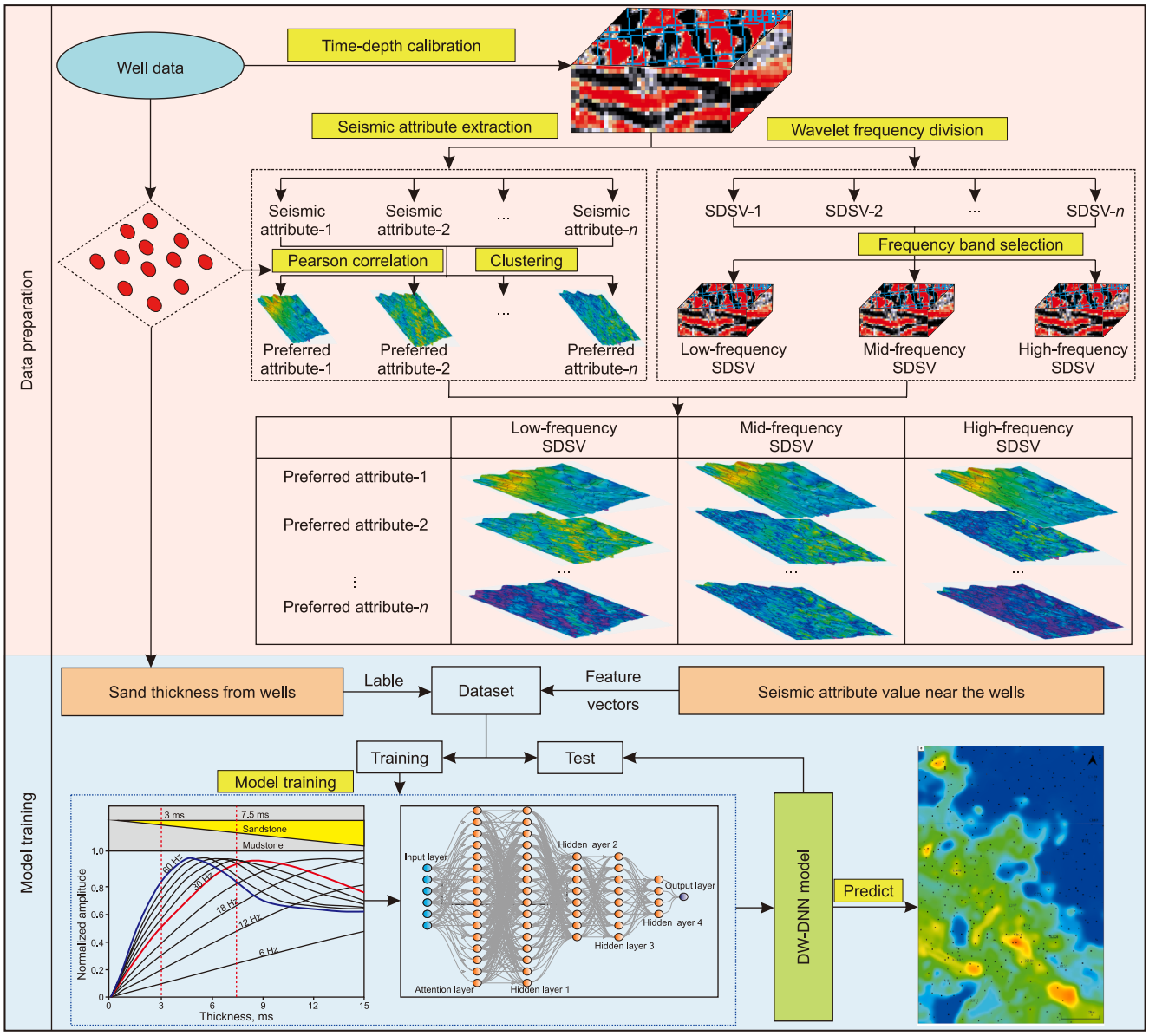

Fig. 1. Workflow of the DW-DNN model for frequency-decomposed attribute fusion (modified from Li et al., 2019a, 2019b). The main change in this paper is the addition of the blue box in the figure. Based on the attention mechanism under physical constraints, the weights of different frequency band attributes are assigned dynamically.

attribute fusion, this paper constructs an a priori weight matrix on the basis of the AVF relationship across various frequency bands. This matrix serves as a guide for training the attention mechanism, enabling a dynamic weight allocation system while adhering to physical constraints. The mechanism is then integrated into a DNN model to increase the accuracy of sand body predictions (Fig. 1).

The tuning relationship between the amplitude and sand thickness at various main frequencies was established by Widess (1973) through forward simulations of a wedge-shaped sand body model. The core principle is that high-frequency seismic waves have a strong tuning effect on thin sand bodies, whereas low-frequency seismic waves have a stronger correlation with thicker sand bodies. Building on this theory, this paper integrates the AVF relationship with a sigmoid function to create an a priori weight matrix.

The core idea of the attention mechanism is to assign weights dynamically on the basis of the importance of the input features. This allows the model to focus on key features while minimizing irrelevant noise. In this work, we apply the attention mechanism to configure weights for seismic attributes across various frequency bands. However, it is difficult for pure data-driven methods to adaptively allocate weights for attributes in each frequency band under different sand thickness conditions because the thickness distribution of sand bodies varies greatly, and the relationship between attributes and sand thickness is affected by multiple geological factors. Thus, it is difficult for data-driven methods to learn their physical laws fully. Therefore, this paper introduces an a priori weight matrix constructed on the basis of the AVF curve as a physical constraint to guide the training of the attention mechanism, forms a dynamic weight allocation mechanism that integrates physical laws, and combines it with a DNN to propose an adaptive weight-controlled frequency-decomposed attribute fusion sand body prediction method (Fig. 1).

The method in this paper achieves reasonable weight allocation through two key technologies: first, an a priori weight matrix is constructed on the basis of the AVF curve and the central frequency of the preferred seismic, and it is embedded in the loss function to constrain the calculation of attention weights,

converting geological laws into trends that guide weight allocation; second, a DNN model guided by the attention mechanism is constructed to extract spatially sensitive features, and the weights of seismic attributes in each frequency band are adaptively adjusted according to the sand thickness of the well point, thereby optimizing the frequency band attribute weight configuration at different sand thickness locations and achieving high-precision sand body prediction.

2.2. Attention mechanism with physical constraints

To facilitate a weight allocation that is both physically informed and spatially adaptive, this study incorporates a prior weight matrix based on the AVF theory. This matrix acts as a physical constraint to guide the training of the attention mechanism within the deep learning framework.

2.2.1. Construction of the prior weight matrix

The fundamental principle of the amplitude versus frequency theory is based on the distinct responses of seismic frequency components to changes in the thickness of sand bodies. High-frequency components, which have shorter wavelengths, exhibit notable tuning effects in thin sand bodies. This is because they effectively capture interference patterns from both the top and bottom reflection interfaces. On the other hand, low-frequency components, which have longer wavelengths and greater penetration depths, are more sensitive to large-scale impedance changes associated with thicker sand bodies (Partyka et al., 1999; Zeng, 2017). When the thickness of the sand body approaches the seismic tuning thickness—defined by Eq. (1), where t represents the tuning thickness, v is the interval velocity, and f is the dominant frequency—there is a nearly linear positive correlation between amplitude and thickness. However, significant deviations from this tuning thickness can lead to nonlinear seismic responses, which may hinder the interpretability of the amplitude attributes (Fig. 2).

The prior weight matrix is structured as a two-dimensional array that captures the AVF-based sensitivity of different seismic frequency bands to varying sand thicknesses. In this matrix, the rows correspond to wells, whereas the columns represent the dominant frequencies of the frequency-decomposed seismic volumes. Each element in the matrix is a weighting coefficient ω, which is calculated via Eqs. (2) and (3), and quantifies the influence of a specific frequency band on the prediction of the sand thickness at a given location. The construction of the prior matrix follows these steps:

The first step in constructing the prior weight matrix is to select optimal low-, medium-, and high-frequency seismic volumes. This process begins by calculating the tuning thickness for a seismic volume with a dominant frequency f via Eq. (1):

$$t = \frac{v}{4f} \tag{1}$$

where t represents the seismic tuning thickness, v denotes the interval velocity obtained from well-log P-wave velocity calibration. For sand bodies with predicted thicknesses within the interval (Y_{min}, Y_{max}), the original broadband seismic volume is decomposed into multiple frequency-decomposed volumes via the continuous wavelet transform (CWT). The dominant frequencies of these volumes range from a minimum of $f = v/(4Y_{min})$ to a maximum of $f = v/(4Y_{max})$, with equal intervals between bands. The number of frequency-decomposed volumes is optimized on the basis of three criteria: (i) the total frequency range should completely cover the original seismic bandwidth to preserve essential spectral information; (ii) each volume must have sufficient bandwidth to ensure a high signal-to-noise ratio; and (iii) redundancy is minimized by selecting the smallest number of frequency bands that satisfy the above conditions (Li et al., 2017).

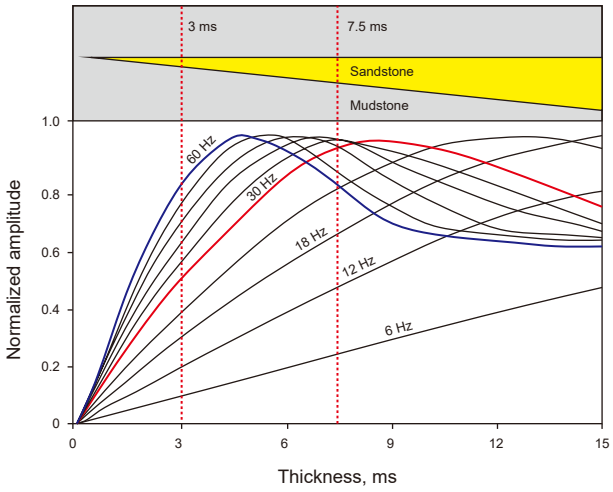

Fig. 2. Forward modeling and tuning curves between the sand thickness and amplitude with different frequency ricker wavelets (AVF) (modified from Li et al., 2019a, 2019b).

Next, the weight correction coefficient ω is defined via a sigmoid function (Fig. 3). For a frequency-decomposed volume with dominant frequency f, its theoretically resolvable sand thickness is denoted as t. When predicting a sand body with an actual thickness y using this volume, the sensitivity of the volume to the sand body can be characterized by the deviation between y and t. Therefore, a thickness deviation index Δy is introduced to quantify the mismatch generated by the frequency-decomposed volume at frequency f when used to predict sand bodies with thickness y.

$$\Delta y = |y - t| \tag{2}$$

The thickness deviation index Δy measures how effectively each frequency-decomposed seismic volume is, where smaller Δy values indicate greater suitability for estimating sand thickness. To account for the varying sensitivities of seismic volumes at different dominant frequencies, a sigmoid function is applied to normalize Δy. This normalization incorporates a sensitivity Factor k ($k > 0$) to control the response range of the function. On this basis, the weight correction coefficient is defined as shown in Eq. (3):

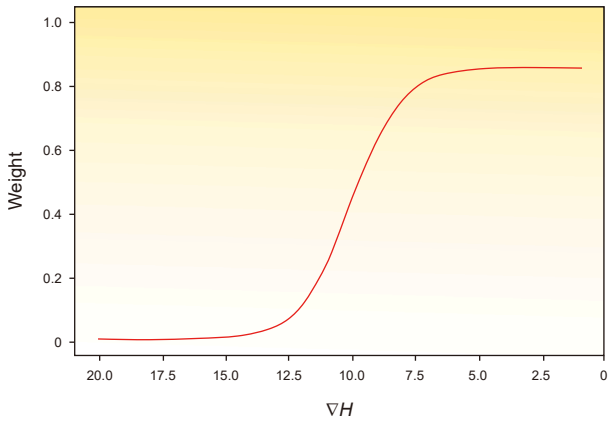

Fig. 3. Sigmoid function curve.

$$\omega = \frac{1}{1 + e^{-k(\Delta y)}} \tag{3}$$

The weight correction coefficient has two fundamental properties:

(i) Nonlinear mapping behavior: the coefficient maps any real-valued input to a range between 0 and 1, allowing its output to be interpreted as a probabilistic weight. This characteristic enables the dynamic allocation of seismic attribute weights across different frequency bands. Compared with linear approaches (such as proportional scaling) and piecewise-defined functions (such as step functions), the sigmoid function offers a smooth and continuous transition, which makes it suitable for gradually adjusting weights in response to changes in the thickness of the sand.

(ii) Central sensitivity mechanism: when the thickness deviation index Δy is extensive, the coefficient approaches zero, effectively diminishing the contributions from frequency bands that are poorly aligned with the target sand thickness. Conversely, when Δy is small, the coefficient approaches one, indicating a high level of confidence in the predictive relevance of the corresponding frequency band (Fig. 3). The sensitivity Factor k ($k > 0$) controls how sharply the weight's response to variations in Δy is. A larger k results in a steeper transition zone, increasing sensitivity to deviations from the tuning thickness. In contrast, a smaller k broadens the transition range, resulting in a smoother and more gradual weighting response.

Finally, the prior weight matrix is constructed, with each well in the target layer represented as a row and the seismic data for various frequency bands represented as columns. For each well, the weight correction coefficients for the seismic data across different frequency bands are calculated via Eq. (3). This process results in the creation of the prior weight matrix. The matrix is then incorporated into the attention mechanism as a physical constraint, guiding the model to prioritize seismic frequency bands that correspond significantly to the sand body.

2.2.2. Training of the attention mechanism

To address the issue of fixed weights for different seismic attributes at each well point, which are commonly used in traditional frequency-decomposed attribute fusion methods, this paper introduces an attention module. This module enables the dynamic configuration of weights for seismic attributes across different frequency bands by leveraging the attention mechanism's ability to adaptively capture long-range dependencies between features and facilitate dynamic interactions among them. However, solely relying on data-driven attention mechanisms for dynamic weight allocation can be challenging. Thus, while maintaining a data-driven approach, this paper introduces the AVF curve, which characterizes the relationship between the amplitude and frequency across various sand thicknesses. By developing a constraint module that incorporates prior geological knowledge into the network training process, the model can dynamically optimize its weight configuration on the basis of the characteristics of sand thickness and frequency band responses. This approach ensures that the analysis is both data driven and informed by the geological context. The construction of attention-based weighting coefficients integrates two complementary components: a data-driven pathway, where neural network parameters are optimized to capture salient features from the input data; and a physics-guided pathway, where prior weights derived from AVF tuning theory are introduced as soft constraints to regulate the learning process, thereby enhancing the physical interpretability and consistency of the model.

The primary function of the attention module is to assign varying weight values dynamically to the seismic attributes across different frequency bands in each well. For each sample, the frequency-band seismic attributes are first fused elementwise with their corresponding AVF prior weights, resulting in a high-dimensional feature representation guided by geophysical priors. This enhanced feature vector is then passed through a three-layer fully connected neural network composed of Dense1–ReLU–Dense2–ReLU–Dense3–Softmax layers. This architecture enables the nonlinear transformation of the fused features into attention weights. The final Softmax activation ensures that the output weights are continuous and differentiable, thereby supporting efficient gradient-based optimization during backpropagation. As illustrated in Fig. 4, the attention module outlined in this paper uses the sand thickness (H) as the supervision target. A nonlinear mapping relationship is constructed between the seismic attributes of each frequency band and the target variable, i.e., the sand thickness, utilizing a trainable parameter matrix (W) and a bias term (b). By employing the backpropagation algorithm for optimization, the module computes the attention score (e) for the seismic attributes of each frequency band via Eq. (4) (LeCun et al., 2015). These scores are then transformed, as indicated in Eq. (5) (Bahdanau et al., 2014), to derive the weight coefficient (α).

$$e = f(X, W, b) = \mathrm{ReLU}(X \cdot W + b) \tag{4}$$

$$\alpha = \mathrm{Softmax}(e) \tag{5}$$

The equation illustrates the feature vector of a given sample, where W represents the trainable weight matrix and b denotes the bias term. The variable e indicates the attention score assigned to the sample, whereas f is the ReLU activation function employed to improve nonlinear feature mapping. The output of the attention module, α signifies the weight coefficients assigned to the frequency-decomposed seismic attributes for each sample.

After generating the initial attention weight matrix, we further enhance the model's physical interpretability and predictive performance by incorporating the prior weight matrix constructed in Section 2.2.1 as a soft constraint. Specifically, at each training iteration, the Euclidean distance squared (i.e., the squared L2 norm) between the current attention weight matrix and the AVF prior weight matrix is computed and embedded into the loss function as a penalty term (Eq. (6)). By minimizing this composite loss function, the model is guided to reduce the discrepancy between the learned attention weights and the AVF-informed prior weights. This encourages the network to learn a physically consistent weight distribution that reflects the known relationship between seismic frequency and sand thickness, thereby improving

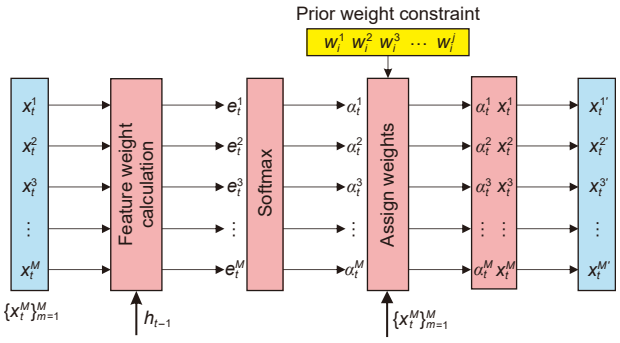

Fig. 4. Attention mechanism workflow with prior weight matrix constraints.

generalization and mitigating overfitting. Furthermore, the constraint strength coefficient λ ($0 \le \lambda \le 1$) is treated as a tunable hyperparameter, whose optimal value is determined through validation set–based hyperparameter tuning to achieve a balance between physical consistency and data-fitting capability.

$$L = \sum (\alpha - \omega)^2 \tag{6}$$

It is crucial to emphasize that the AVF-based prior weights, which are introduced as a soft physical constraint, serve as a complement rather than a hard limitation. These weights are integrated into the total loss function as a tunable penalty term, with their influence regulated by a weighting coefficient λ. In this framework, the AVF prior acts as a supplementary guide, promoting geophysically consistent learning without superseding the optimization pathway dictated by the data itself. This design philosophy ensures that the training process remains predominantly data-driven. In contexts where the actual seismic response markedly deviates from the ideal AVF tuning relationship—such as in the presence of significant noise, intricate geological structures, or target layers that lie beneath the resolution of the tuning thickness—the model has the capacity to adaptively modify the attention weight distribution via the backpropagation mechanism. This ability enables the network to accentuate features that align more closely with the observed data, thereby retaining its adaptability to the complexities of real-world scenarios while ensuring physical interpretability.

Ultimately, the attention weight coefficient obtained after iterative optimization is multiplied elementwise by the seismic attributes of each frequency band to create a new feature set X', as illustrated in Eq. (7).

$$X' = \alpha \cdot X \tag{7}$$

This section uses the i-th well point, X_i, as an example to explain the process of reconstructing sample features. Let X_i^j represent the j-th seismic attribute value of the i-th well point, and let β_i^j denote its corresponding dynamic weight. The feature reconstruction process is illustrated in Fig. 4. In this diagram, the weights for each feature are calculated first. These weights are then assigned to their corresponding features via Eq. (8). Finally, the reconstructed sample features X_i' are generated.

$$X_i' = \left[\left(x_i^1\right)', \left(x_i^2\right)', \left(x_i^3\right)', \cdots, \left(x_i^j\right)'\right] = \left[x_i^1 \times \beta_i^1, x_i^2 \times \beta_i^2, \cdots, x_i^j \times \beta_i^j\right] \tag{8}$$

2.3. Frequency-decomposed attribute fusion method using DW-DNN

A DNN typically consists of multiple fully connected layers, with nonlinear activation functions (e.g., ReLU, sigmoid) enabling the gradual extraction of hierarchical features (LeCun et al., 2015). Lower layers capture local features, whereas higher layers construct global representations, making DNNs suitable for modeling complex data distributions (Jeffrey, 2018; He et al., 2016). The basic architecture of a standard DNN includes an input layer, one or more hidden layers, and an output layer. In this paper, we propose a DNN model enhanced with an attention mechanism that operates under physical constraints, resulting in what we call a DW-DNN model. This model consists of four modules: the input layer, the attention module, the hidden layer, and the output layer (Fig. 5).

The input layer processes a multidimensional matrix of seismic attributes, containing M frequency-decomposed attributes from N well points, with neuron count equal to M. To address discrepancies across frequency bands, the input undergoes Z-score standardization, reducing anomalies from differences between high- and low-frequency attributes (e.g., instantaneous frequency vs. wave impedance). The standardized input $h^{(0)} = x$ is passed through a fully connected layer to the attention module, enabling feature space reconstruction and sequential mapping to the output y via nonlinear activation at each hidden layer. The forward propagation process is expressed in Eq. (9). The attention module implements dynamic weight allocation in three steps. (a) Feature Importance Calculation: a fully connected layer performs nonlinear mapping on attribute features to generate importance scores, indicating each frequency band's contribution to sand thickness, learned through backpropagation. (b) Probability Distribution Conversion: the scores are transformed into a probability distribution via the Softmax function, ensuring interpretability and integration of contributing factors. (c) Prior Weight Integration: prior weights derived from physical constraints are incorporated, and the deviation between attention weights and prior weights is optimized through a loss function, enabling dynamic adjustment consistent with physical principles. The hidden layer, with a hierarchical architecture, employs a combined regularization strategy to optimize nonlinear extraction of high-dimensional features and improve generalization. It adopts a four-layer fully connected structure with 256, 128, 128, and 64 neurons, enabling progressive feature transformation. The choice of network depth and neuron counts was determined through ablation studies, where different configurations were evaluated on a validation dataset to balance model capacity and computational efficiency. The first two layers (h1 and h2) use dropout regularization with a 0.2 rate to reduce overfitting from high-frequency noise and enhance robustness. The last two layers (h3 and h4) apply batch normalization to standardize activation outputs, reducing gradient fluctuations and improving convergence stability. The dropout rate was set to 0.2 after testing several values (0.1, 0.2, 0.3 ….0.6), as it provided the best trade-off between preventing overfitting and retaining sufficient information for learning meaningful patterns. Similarly, the decision to apply batch normalization after the last two hidden layers was based on experimental observations that it most effectively stabilized training dynamics in the latter stages of the network. Together, these techniques form a dynamic optimization mechanism, where shallow layers enhance feature robustness and deeper layers ensure distribution consistency. The output layer maps the high-dimensional features extracted by the hidden layer to the predicted sand thickness. As a regression task, it consists of a single neuron, whose output directly represents the predicted thickness for each sample based on processed features.

$$y = f\left(h^{(L)}, \theta^{(L)}, \alpha^{(L)}\right) = f^{(L)}\left(H^{(L-1)}\right) \tag{9}$$

In the equation, L represents the total number of layers within the model, $f\left(h^{(L)}\right)$ represents the activation function of the L-th layer, $f^L(\theta)$ represents the weight matrix of the L-th layer, and $f^L(\alpha)$ represents the bias term of the L-th layer.

The loss function is defined as a linear combination of the prediction error and the AVF constraint. The prediction error uses mean squared error (MSE) to measure the deviation between predicted and actual sand thickness, while the AVF constraint evaluates the discrepancy between attention weights and AVF-derived prior weights. During training, this loss guides parameter updates through backpropagation, optimizing both weight allocation and prediction accuracy. Thus, the model learns to assign weights to frequency-decomposed seismic attributes

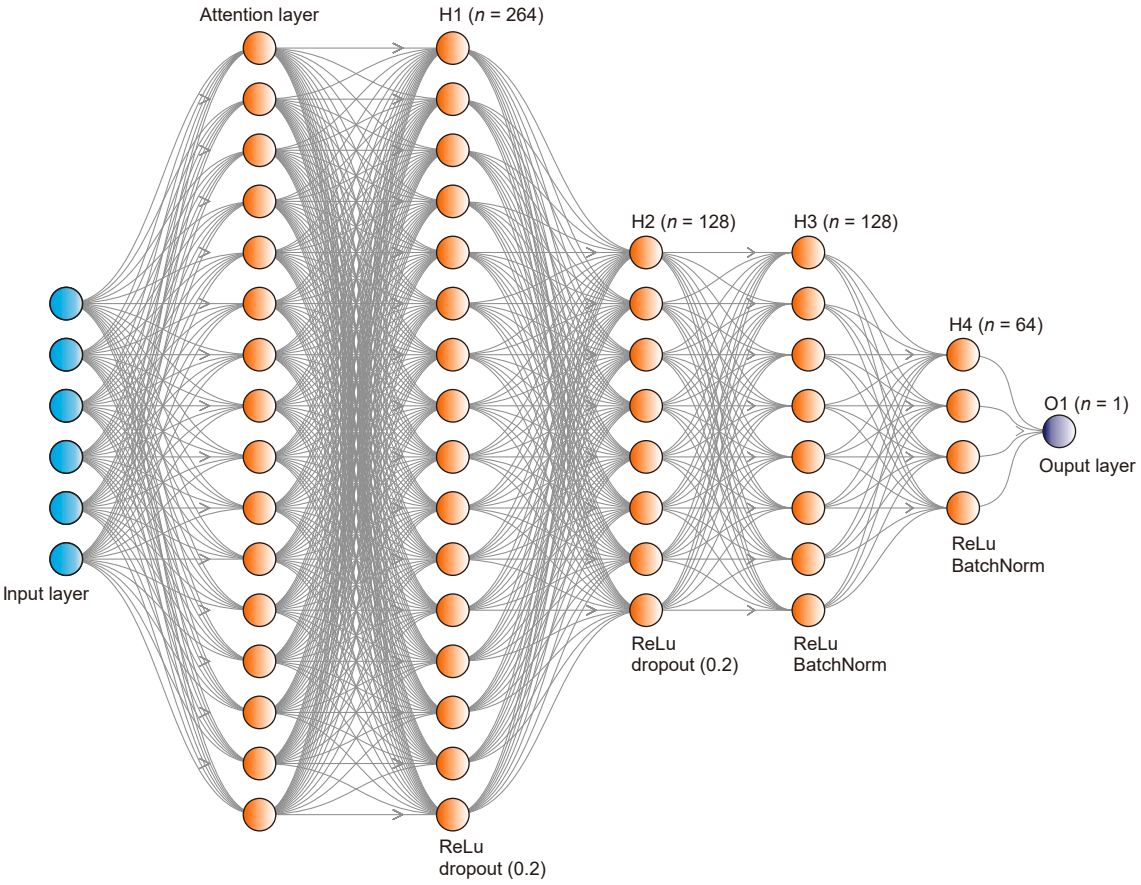

Fig. 5. Architecture of the DW-DNN.

according to sand thickness characteristics, thereby reducing prediction error. The formulation is expressed as follows:

$$L = \frac{1}{N}\sum_{i=1}^{N}(\widehat{Y}_i - Y_i) + \lambda\sum_{i=1}^{N}\sum_{j=1}^{M}\left(\alpha_{i,j} - \omega_{i,j}\right)^2 \tag{10}$$

where Y_i denotes the actual sand thickness of the i-th sample and where $\widehat{Y}_i$ represents the predicted sand thickness of the same sample. Furthermore, $\alpha_{i,j}$ represents the dynamic weight of the j-th attribute associated with the i-th well point, as learned by the attention mechanism, and $\omega_{i,j}$ represents the prior weight computed on the basis of AVF tuning theory. λ represents the constraint strength coefficient, which is explicitly employed to regulate the weight ratio of the AVF constraint within the total loss function.

3. Method application

Frequency-separation attribute fusion refers to the process of integrating multiple individual attributes to interpret sand bodies. This process begins with the selection of effective seismic frequency bands and seismic attributes that strongly correlate with the sand thickness. We subsequently extract seismic attributes from various frequency bands of bypass well data to construct a dataset. Via the DW-DNN approach, these seismic attributes from distinct frequency bands are fused to generate a composite set of attributes. The resulting fused attributes are employed as collaborative data in conjunction with a well-controlled interpolation technique to delineate the distribution of the sand thickness at the sand group level.

As a case study, this paper takes the third sand group of the Xi 233 area of the Qingcheng Oilfield in the Ordos Basin as an example to explain the frequency-separation attribute fusion process based on the DW-DNN method and prove the effectiveness of the method in actual work areas.

3.1. Study area setting

The Ordos Basin, located in the western region of the North China Craton and encompassing the provinces of Shaanxi, Gansu, and Ningxia, is characterized as a multicycle superimposed basin (Fig. 6(a)). This basin is further classified into six primary tectonic units, namely, the Weibei Uplift, Yishan Slope, Jinxi Flexural Fold Belt, Yimeng Uplift, Tianhuan Depression, and West Margin Thrust Belt (Liu et al., 2007; Yang et al., 1992; Zhao, 2004), and encompasses a total area of approximately 37 $\times$ 10^4 km^2 (Fig. 6(b)). The current study focuses on the Xi 233 area of the Qingcheng Oilfield, which occupies an area of 832 km^2 and is located in the southwest region of the Yishan Slope. This area is a significant oil-bearing region within the Changqing Oilfield, with the middle section of the Triassic Yanchang Formation identified as the primary oil-bearing stratum. Recent research suggests that the internal stratigraphic structure of this formation is characterized by a "progradation-unequal thickness" style, allowing it to be subdivided into ten distinct sand groups. The shallow water zone within this area is characterized predominantly by the development of deltas, whereas the slope zone features gravity flow channels that are distributed in narrow strips along the slope. Additionally, gravity flow lobes are observed at the proximal end of the basin bottom zone, which contrasts with the

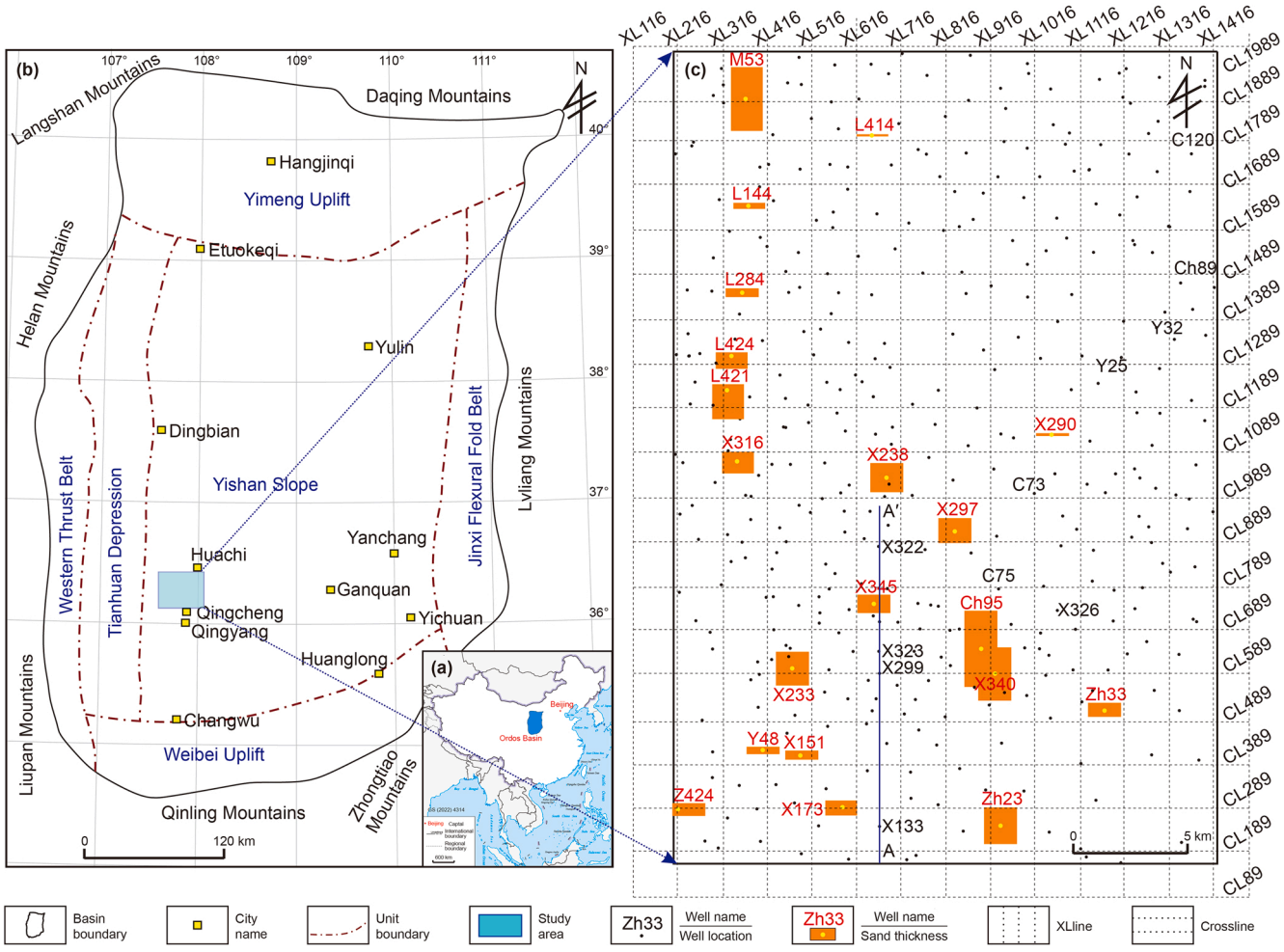

Fig. 6. **(a)** Geological–structural location. **(b)** Distribution of tectonic units and location of the study area. **(c)** Well distribution in the study area (exploratory and appraisal wells), the average well spacing is 1500 m. The orange rectangular height in the figure indicates the thickness of the sand body at the well point. The higher the height, the thicker the sand body, In the figure, "CL" should be the abbreviation for "Crossline", and "XL" should be the abbreviation for "Inline".

deposition of deep lake mud shale, primarily at its distal end (Lyu et al., 2022, 2025; Liu et al., 2025).

All data used in this study were provided by the PetroChina Changqing Oilfield Company. Three-dimensional seismic data were acquired in the Xi 233 area, covering an area exceeding 832 km^2, with the seismic grid shown in Fig. 6. The dataset consists of 1940 inlines (inline range: 116–1416) and 1380 crosslines (crossline range: 89–1989), with 1501 samples per trace at a 2 ms interval. The seismic volume has a central frequency of about 37 Hz and an effective frequency band ranging from 11 to 63 Hz (Fig. 7(a)). Interval velocities in the study area vary from 3500 to 4000 m/s, and the vertical resolution is approximately 27 m. A total of 364 wells (exploration and appraisal wells) have been drilled in this block, with an average well spacing of 1500 m (Fig. 6(c)). The logging data, which include natural gamma logging (GR), acoustic time difference logging (AC), density logging (DEN), and natural potential logging (SP), contribute to a comprehensive understanding of subsurface characteristics, there are 47 wells with incomplete logs. Furthermore, the cumulative length of cores extracted from nine coring wells is 495 m. An analysis of the distribution characteristics of the sand bodies in the study area was conducted on the basis of the sand thicknesses interpreted from core and logging data. Taking the third sand group as a representative example, there are 317 wells drilled in the third sand group with complete logging curves. The thickness of the sand within this formation predominantly ranges from 1 to 20 m, with the thinnest sand measuring 1.2 m and the thickest reaching 38 m (Fig. 7(b)). This significant variability in sand thickness, along with the heterogeneous planar distribution of the sand bodies (Fig. 6(c)), presents considerable challenges for accurate predictions regarding their extent and characteristics.

3.2. Data processing

3.2.1. Seismic frequency band selection

Numerous studies have shown that tuning effects and resolution impact the interpretation of seismic data. High-frequency seismic data are particularly effective in characterizing thin sand bodies, whereas medium- and low-frequency data are more appropriate for predicting thicker sand bodies (Li et al., 2019a, 2019b; Zeng and Backus, 2005). Consequently, conducting a multiband analysis of seismic data has the potential to increase the accuracy of sand body prediction.

The original seismic data were decomposed into a series of spectral components, referred to as spectral-decomposed seismic volumes (SDSVs), through spectral decomposition. To perform this, the Continuous Wavelet Transform (CWT) was employed, as it enables effective capture of localized signal variations across both

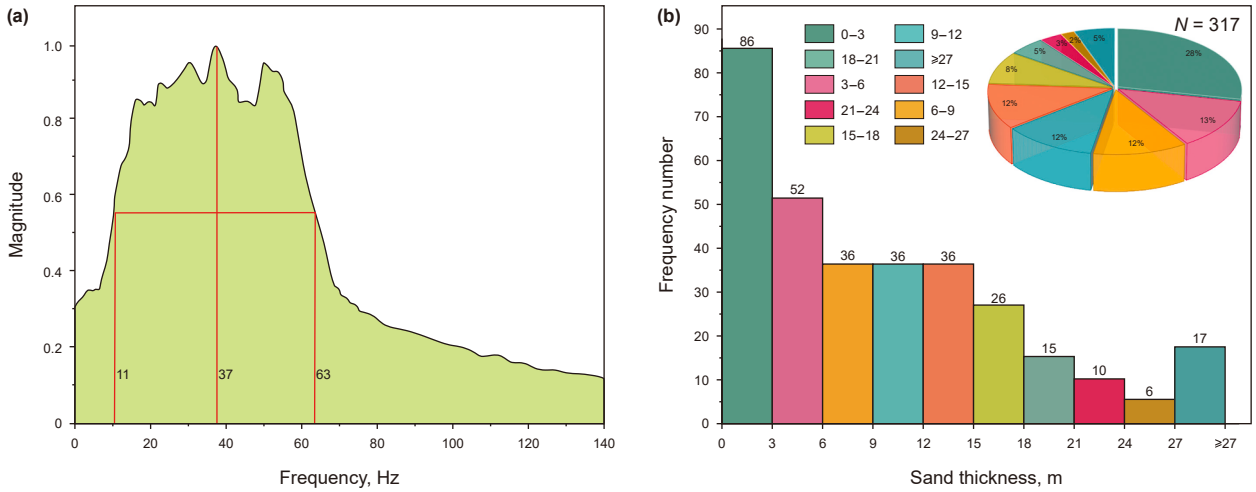

Fig. 7. Data overview of the study area. **(a)** Normalized frequency of the original seismic cubes of the Chang 7 Member in the study area. The 3D seismic cubes have a dominant frequency of 37 Hz and a bandwidth of 11–63 Hz, **(b)** sand thickness from wells distribution histogram and pie chart of the third sand group in the study area, the thickness of the sand within this formation predominantly ranges from 1 to 20 m, with the thinnest sand measuring 1.2 m and the thickest reaching 38 m.

temporal and frequency dimensions. Its capacity to balance time and frequency resolution—providing high temporal resolution at low frequencies and vice versa—makes it particularly suitable for analyzing non-stationary seismic signals (Li et al., 2019a, 2019b; Sinha et al., 2005). In this study, the CWT, utilizing Marr wavelets as the mother wavelet, was applied to generate SDSVs characterized by distinct dominant frequencies and bandwidths. The original seismic data are processed via a wavelet frequency division technique based on 5 Hz equidistant frequency intervals. A corresponding tuning thickness table is established via Ricker wavelet theory (Table 1). Selection criteria were primarily based on the relationship between the tuning thickness of seismic data and the actual sand body thickness. Specifically, the tuning thickness of the lowest-frequency seismic volume should be sufficient to capture the thickest sand bodies, while that of the highest-frequency volume should approach the thinnest ones.

For the third sand group, the maximum sand body thickness reaches 38 m, which corresponds to a tuning thickness of 43.1 m for the low-frequency seismic volume with a dominant frequency of 20 Hz. This allows for effective imaging of thick sand bodies. However, most sand bodies in the Xi 233 area are relatively thin, with thicknesses ranging from 1 to 20 m and a minimum of 1.2 m. Even at the highest dominant frequency (55 Hz), the tuning thickness still significantly exceeds the thickness of the thinnest sand layers. To enhance the detection of such thin beds, high-frequency components were prioritized during frequency selection to improve resolution. Meanwhile, overall data redundancy was reduced through careful selection of the frequency bands. Ultimately, four optimized and representative seismic frequency volumes were selected to comprehensively cover the original seismic bandwidth while preserving key resolution characteristics. These include a low-frequency volume centered at 20 Hz (Fig. 8(a)), a medium-low frequency at 35 Hz (tuning thickness: 28.5 m; Fig. 8(b)), a medium-high frequency at 45 Hz (tuning thickness: 26.5 m; Fig. 8(c)), and a high-frequency volume at 55 Hz (tuning thickness: 23 m; Fig. 8(d)). This configuration minimizes spectral redundancy, preserves essential amplitude information, and establishes a solid foundation for subsequent multiband feature fusion.

Taking the sum of the amplitude attributes as a case (Fig. 9), low-frequency data exhibit lower resolution, resulting in a more compressed representation of the high-value areas and a stronger response to thick sand bodies (Fig. 9(a)). High-frequency data display higher resolution, allowing for a finer delineation of high-value boundaries and increased sensitivity to thin sand bodies (Fig. 9(d)); however, these data may experience attenuation in regions characterized by thick sand bodies. Moreover, the medium-frequency data demonstrate intermediate characteristics, effectively balancing sensitivity to both thin and thick sand bodies (Fig. 9(b)–(c)).

3.2.2. Seismic attribute selection

Different seismic attributes demonstrate varying degrees of sensitivity to the responses of sand bodies (Yue et al., 2022; Zeng, 2010). Consequently, the selection of seismic attributes that exhibit heightened sensitivity to variations in sand thickness becomes imperative. The process of attribute selection integrates mathematical statistics with geophysical principles to identify those attribute combinations that strongly correlate with sand thickness. This process can be divided into two fundamental steps: first, attributes that are significantly correlated with the sand thickness are extracted from the original seismic data via the Pearson correlation coefficient; second, to increase the effectiveness of the attribute combination, collinear attributes are removed via feature similarity analysis.

By utilizing the advantages of the original seismic data, which contain a relatively comprehensive set of information, a total of 14 well-side seismic attributes were extracted from 317 wells. The Pearson correlation coefficient was subsequently computed for each seismic attribute in relation to the thickness of the sand at

Table 1
Tuning thickness analysis of the frequency-decomposed data volume.

Center frequency, Hz	15	20	25	30	35	40	45	50	55
Dominant frequency, Hz	19.5	23.5	27.5	31.5	35.5	37.5	39.5	43	45
Tuning thickness, m	51.9	43.1	36.8	32.1	28.5	27	26.5	23.6	23

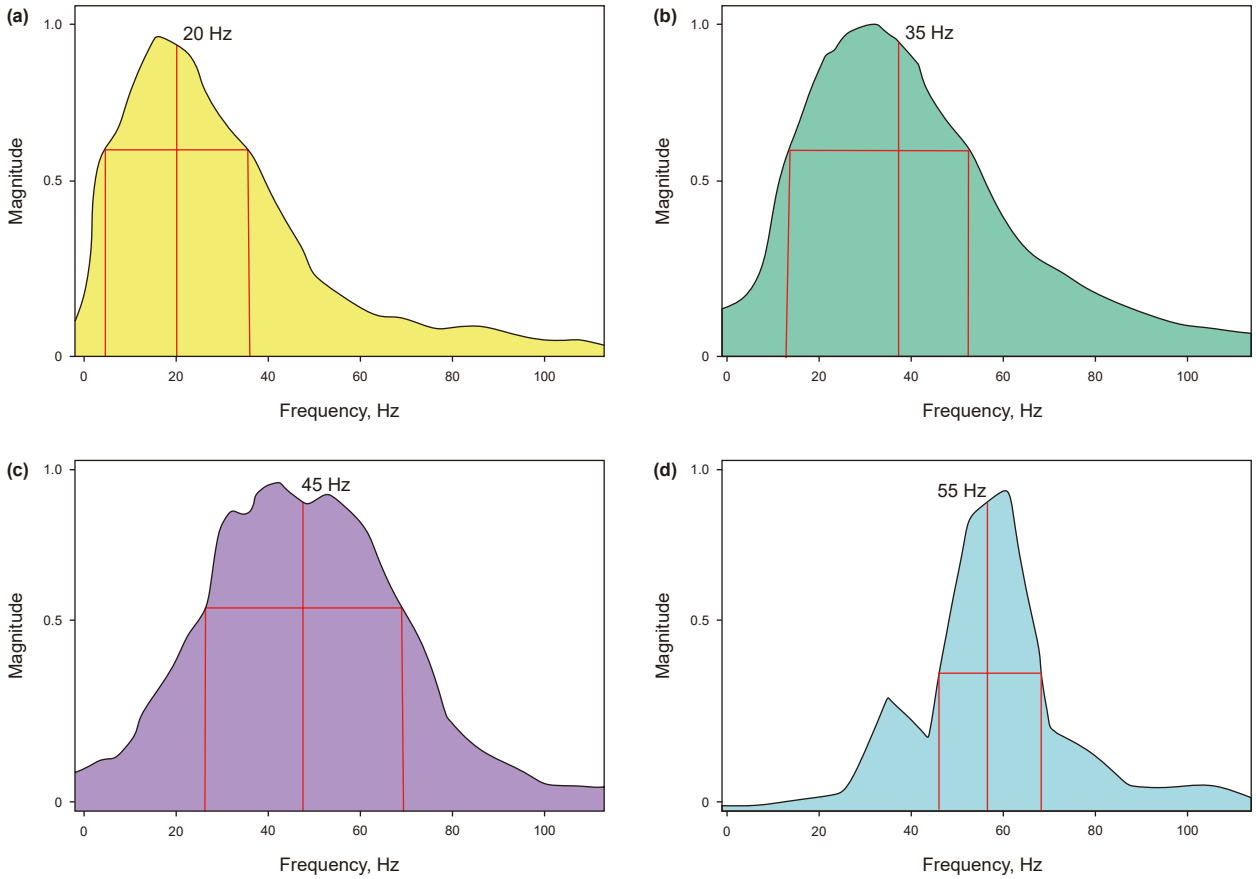

Fig. 8. Frequency spectrum of the divided seismic cubes in the study area, **(a)** low frequency (20 Hz), **(b)** mid–low frequency (35 Hz), **(c)** mid–high frequency (45 Hz), **(d)** high-frequency (55 Hz).

each well (Table 2). Among these, eight seismic attributes exhibited correlation coefficients exceeding 0.35. To address potential collinearity among the attributes, these eight seismic attributes were subjected to hierarchical clustering, resulting in their classification into three distinct categories (Fig. 10). Following the principle of "maximizing feature representation while minimizing information duplication", a single representative attribute was chosen for each category of seismic attributes. Consequently, the isochronous thickness attribute, average trough value attribute, and root mean square amplitude were selected as the final attributes. Ultimately, these three attributes were extracted from four frequency-decomposed data volumes, thereby constructing a dataset that comprises 12 seismic attributes along with the corresponding thickness of the sand body at the wells, which is intended for subsequent model training.

3.3. Intelligent attribute fusion and evaluation

3.3.1. Model training

This paper constructs an adaptive weighted deep neural network model (DW-DNN) based on the TensorFlow deep learning framework to perform nonlinear modeling of seismic attributes within each frequency band and sand thickness at designated well points. Using a random partitioning strategy, 70% of the wells (221 wells) are designated training wells, during training, 10% of the training wells were further held out as a validation set for hyperparameter tuning. The remaining 30% (96 wells) are employed as blind wells to assess the model's generalization ability. The key hyperparameters are configured as outlined in Table 3. The learning rate follows a piecewise decay strategy, which maintains a high update rate during the initial rapid decline phase and reduces the fluctuation amplitude in the subsequent fine-tuning stage. To mitigate the risk of overfitting, the L2 regularization coefficient is implemented, and the batch size is optimized to balance computational efficiency with gradient stability. Moreover, the training cycle dynamically determines the optimal number of iterations by employing the early stopping method. In terms of the optimization strategy, the model formulates the loss function with the mean square error (MSE) as its core component and incorporates a constraint term derived from AVF tuning theory, resulting in a composite loss function. The Adam optimizer is used to adaptively adjust the learning rate, optimize the network parameters, and accelerate the convergence process.

The final training loss curves are illustrated in Fig. 11, which delineates the evolution of three distinct components: the prediction loss represented by the mean squared error (MSE-loss), the attention loss derived from the AVF-based prior weighting mechanism (attention-loss), and the composite loss formed by the weighted summation of the two (total-loss). During the initial training stage (first 50 epochs), the model undergoes a rapid convergence phase, with the total loss decreasing by approximately 82%, indicating a significant improvement in fitting efficiency. In this phase, the MSE-loss exhibits a steep decline, reflecting the rapid enhancement of predictive accuracy, while the attention-loss decreases at a relatively slower yet consistent rate, signifying stable learning of prior physical constraints. As training progresses into the mid-to-late stage (epochs 150 to 350), all three loss curves gradually converge. The total-loss demonstrates

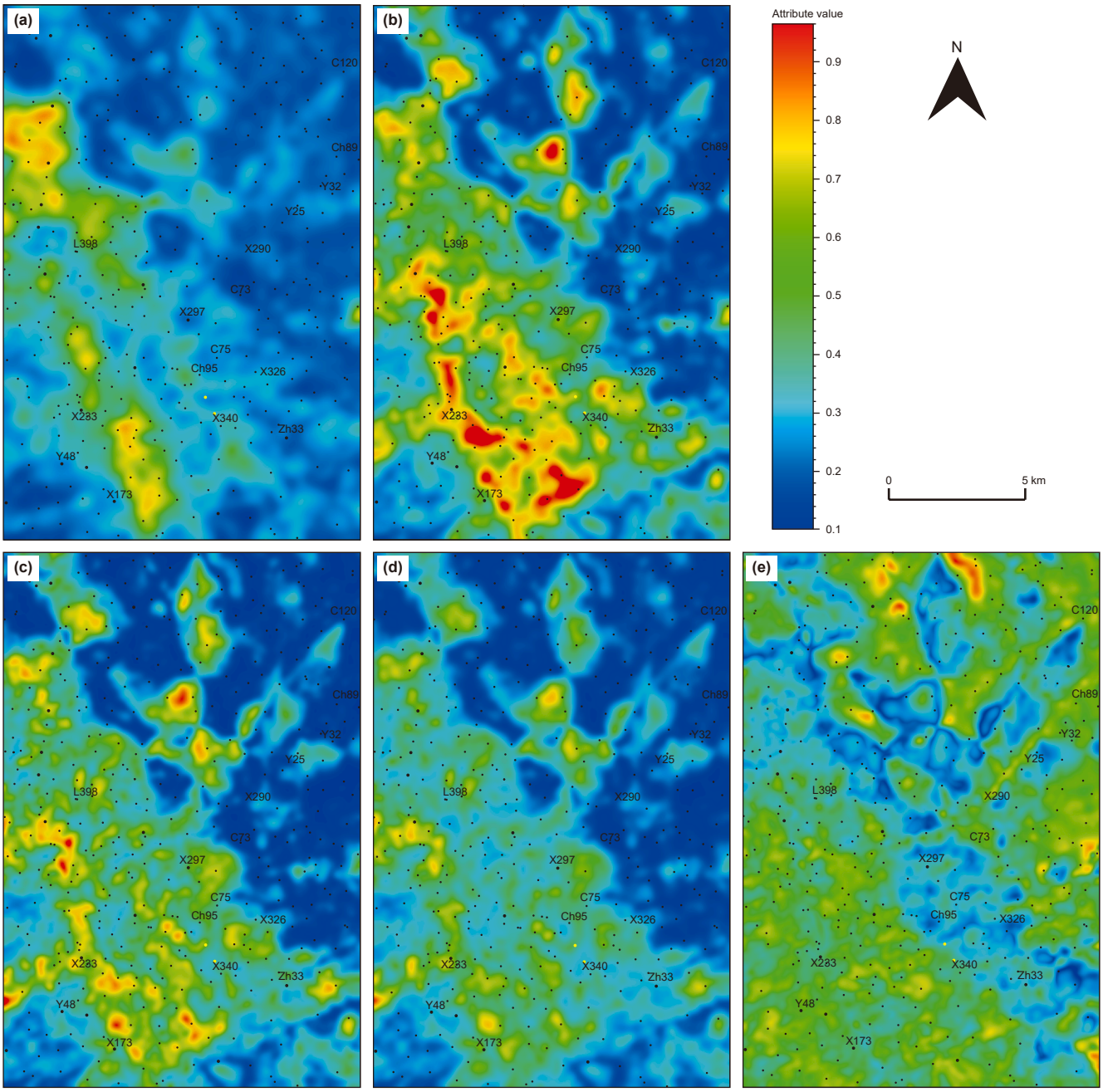

Fig. 9. Multifrequency average trough amplitude attribute maps of the third sand group in the study area, **(a)** 20 Hz average trough amplitude, **(b)** 35 Hz average trough amplitude, **(c)** 45 Hz average trough amplitude, **(d)** 55 Hz average trough amplitude, **(e)** full-frequency band average trough amplitude.

Table 2
Correlation coefficients between each seismic attribute and the sand thickness, the names of seismic attributes in bold indicate higher correlation, which will be used for further clustering selection.

Attribute name	Correlation (R)	Attribute name	Correlation (R)
Isochron thickness (IT)	0.51	Minimum amplitude (MinA)	0.34
Average trough value (ATV)	0.47	Maximum magnitude (MaxM)	0.32
Average negative trough value (ANTV)	0.45	Time at maximum amplitude (T_{max}A)	0.31
Mean amplitude (MEA)	0.43	Half energy (HE)	0.31
RMS amplitude (RMS)	0.39	Time at minimum amplitude (T_{min}A)	0.26
Average magnitude (AM)	0.39	Sum of magnitudes (SM)	0.17
Average negative amplitude (ANM)	0.39	Sum of energy (SOE)	0.11
Average energy (AE)	0.38	Average positive amplitude (APA)	0.11
Sum of positive amplitudes (SPA)	0.35	Sum of negative amplitudes (SNA)	0.08
Sum of amplitudes (SOA)	0.34	Maximum amplitude (MaxA)	0.06

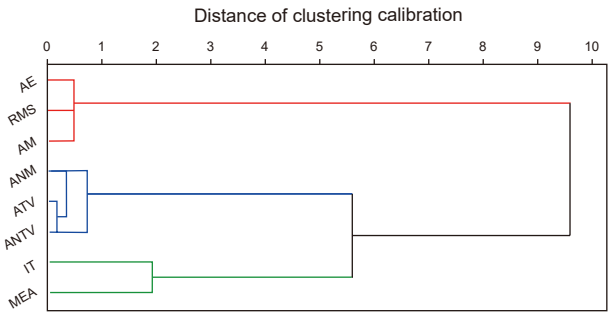

Fig. 10. Dendrogram of the selected seismic attributes via hierarchical cluster analysis, the red lines indicate cluster 1, the blue lines indicate cluster 2, and the green lines indicate cluster 3, the full names of the seismic attributes are shown in Table 2.

Table 3
Model hyperparameter configuration.

Parameter name	Value	Type	Function description
Learning rate (η)	0.001	Optimizer	Controls the step size during gradient descent
L2 regularization coefficient (λ)	0.01	Regularization	Penalizes large weights to mitigate overfitting
Rraining epochs	350	Stopping	Determined by early stopping criteria
Batch size	32	Optimization	Balances memory usage with model convergence
Dropout rate (p)	0.2	Regularization	Randomly deactivates neurons during training

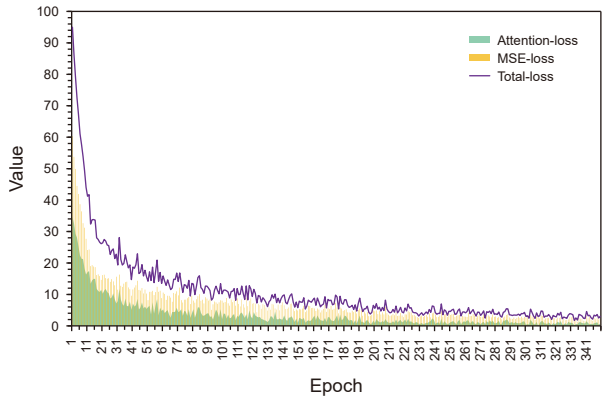

Fig. 11. Loss curves during model training, the total loss declines rapidly in the early epochs and stabilizes after approximately 200 epochs, at around epoch 350, all losses converge, with attention-loss reaching its minimum, indicating optimal alignment between data-driven prediction and AVF prior weighting.

reduced fluctuations and stabilizes progressively, while the attention-loss continues to decline and remains at a consistently low level, suggesting that the attention weights have reached a rational and stable distribution. Notably, around epoch 350, when the total-loss attains its minimum value (approximately 1.05–1.08), the attention-loss also reaches its lowest point. This convergence implies that the model not only achieves optimal predictive performance but also successfully adapts the prior-informed attention weights, thereby attaining a balance between data-driven learning and physical consistency (Fig. 11).

3.3.2. Evaluation of the sand thickness predictions at the well points

The prediction outcomes related to the thickness of the well-point sand bodies serve as a quantitative basis for assessing the accuracy and reliability of the proposed model. This study employs several metrics, namely, the root means square error (RMSE), mean absolute error (MAE), and determination coefficient (R^2), to comprehensively evaluate the prediction accuracy. Specifically, the RMSE reflects the overall distribution characteristics of the prediction error; the MAE indicates the absolute magnitude of the error; and R^2, which ranges from 0 to 1, reflects the strength of the relationship between the independent variable and the dependent variable in the regression analysis. A value closer to 1 signifies a more substantial explanatory effect. The calculation formulas for each of these indicators are provided in Eq. (11) through (13).

$$\mathrm{RMSE} = \sqrt{\frac{1}{n}\sum_{i=1}^{n}(y_i - \hat{y}_i)^2} \tag{11}$$

$$\mathrm{MAE} = \frac{1}{n}\sum_{i=1}^{n}|y_i - \hat{y}_i| \tag{12}$$

$$R^2 = 1 - \frac{\sum_{i=1}^{n}(y_i - \hat{y}_i)^2}{\sum_{i=1}^{n}\left(y_i - \bar{y}_i\right)^2} \tag{13}$$

In this context, n denotes the number of well points. The term $\hat{y}$ refers to the sand thickness as interpreted from well logging data, whereas y_i represents the predicted sand thickness at the i-th well point. Additionally, $\bar{y}_i$ signifies the average value of the sand thickness derived from well logging observations.

Based on the trained model, multiple attributes of the study area are fused to obtain the fusion seismic attribute map. A quantitative evaluation of the blind-well prediction results revealed a high correlation between the seismic attribute fusion outcomes and the thickness of the sand, as evidenced by a determination coefficient (R^2) of 0.92 (Fig. 12(a)). The intelligent fusion attribute has a robust correlation with the thickness of the sand, effectively reflecting both its distribution trend and characteristic features. The results of this prediction align with the sand thickness inferred from well logging and mirror the distribution trend of the intelligent fusion attribute. Overall, the sand bodies of the third sand group are predominantly concentrated in the southwestern region, in proximity to the provenance area, with their thickness gradually decreasing toward the northeast (Fig. 13(a)). These sand bodies are distributed in a continuous manner. The prediction error across all the well points remains below 6 m. A statistical analysis categorized by thickness interval reveals that the average errors are as follows: 2.1 m for the 0–3 m thickness interval, 1.8 m for the 3–6 m interval, 1.5 m for the 6–9 m interval, 1.4 m for the 9–12 m interval, 1.1 m for the 12–15 m interval, 1.2 m for the 15–18 m interval, and an average error of 0.65 m for sand bodies exceeding 18 m. Notably, the prediction error diminishes progressively with increasing sand thickness (Fig. 14), leading to an overall prediction accuracy that significantly surpasses the seismic vertical resolution. This phenomenon occurs because the model has learned the weight distribution mechanism under physical constraints. In regions characterized by thicker sand bodies, the model primarily allocates weight to low-frequency (20–35 Hz) attributes, thereby fully exploiting the response of low-frequency seismic attributes in relation to substantial sand bodies (Fig. 12(b)). For example, the measured thickness of the sand in CH95 Well is 25.80 m (Fig. 13(b)), whereas the predicted result is 25.56 m, yielding a prediction error of only 0.24 m, in Z57 Well, the thickness is 23.00 m, and the predicted thickness is 22.77 m, resulting in a prediction error of 0.23 m; likewise, for zh23 Well,

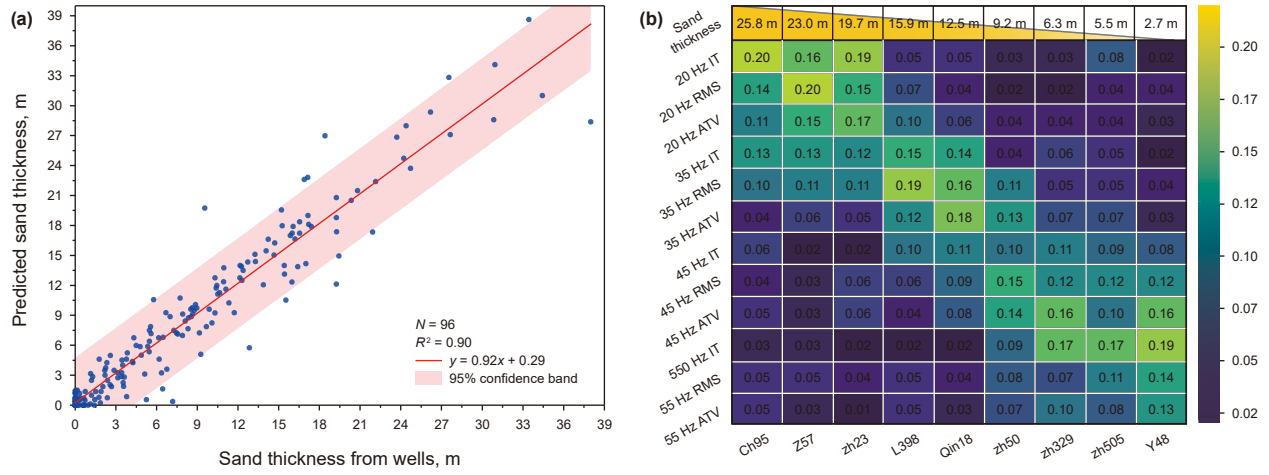

Fig. 12. **(a)** Comparison of the predicted and true values on the test set ($R^2 = 0.92$), **(b)** blind-well weight distribution, single well frequency attribute weight distribution. In areas characterized by thick sand bodies, the model predominantly emphasizes low-frequency attributes (20–35 Hz), in areas with thin sand bodies, it tends to focus on medium to high-frequency attributes (45–55 Hz).

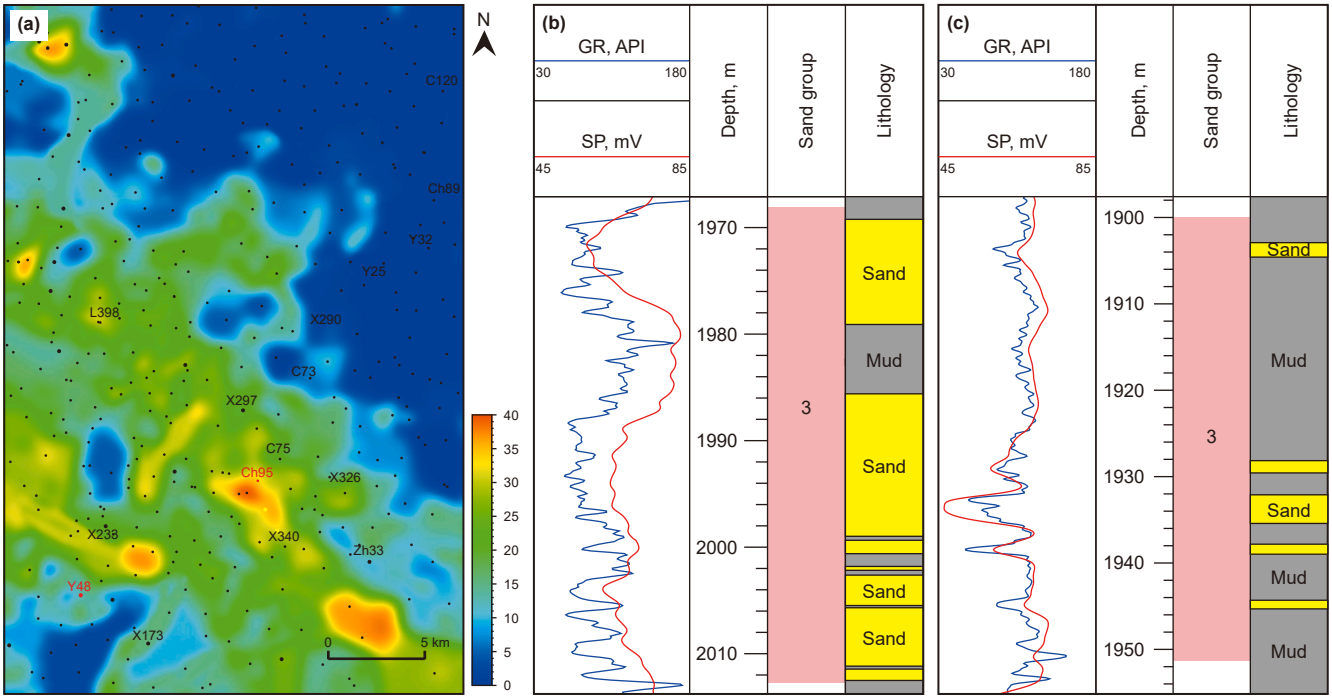

Fig. 13. Prediction of sand body thickness distribution results, **(a)** prediction results based on DW-DNN model, **(b)** logging characteristics for the Ch95 well, **(c)** logging characteristics for the Y48 well.

the thickness is 19.70 m, and the model predicts 20.36 m, which corresponds to a prediction error of 0.66 m. Importantly, the prediction errors for these sand bodies are consistently low. Conversely, in locations with thinner sand bodies, the model favors medium- and high-frequency (45–55 Hz) attributes, thereby enhancing its ability to focus on high-frequency seismic attributes in these areas. For example, at the L398 well, the sand thickness is 15.9 m, with a predicted result of 16.35 m, resulting in a prediction error of 0.55 m; at the zh50 well, the thickness is 9.20 m, whereas the predicted thickness is 9.72 m, leading to a prediction error of 0.62 m; and at the zh329 well, the measured thickness is 6.3 m, and the predicted result is 6.35 m, yielding a minimal prediction error of 0.05 m, and at the Y48 well, the measured thickness is 2.7 m, and the predicted result is 3.45 m, yielding a minimal prediction error of 0.75 m (Fig. 13(c)). Overall, these small prediction errors reflect the model's successful learning of a rational weight allocation mode throughout the training process.

3.3.3. *Types and distribution characteristics of sedimentary microfacies*

Previous research conducted in the Xi 233 area has extensively explored sedimentary microfacies. The provenance of the third section of the Yanchang Formation, situated in the Xi 233 area, is sourced from the southwest (Liu et al., 2015; Liang et al., 2022). Six types of sedimentary microfacies were recognized, including channel, main channel, distributary channel, levee–overbank,

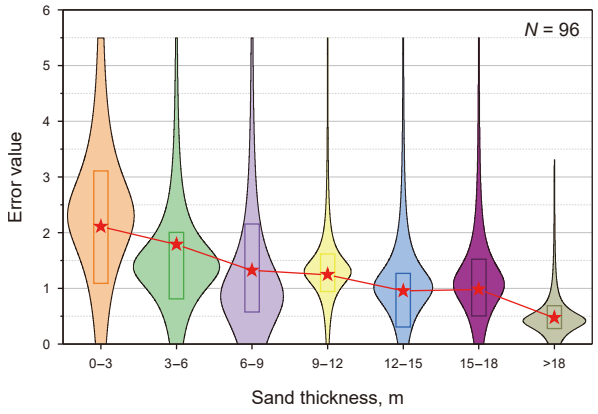

Fig. 14. Error distribution map for different sand thicknesses, the prediction error diminishes progressively with increasing sand thickness.

mouth bar, and lobe (Li et al., 2023; Liu et al., 2025; Zhu et al., 2013).

Based on these foundational studies, this paper clarifies the characteristics and distribution patterns of each sedimentary microfacies, utilizing sand body thickness distribution along with core and logging interpretation data to enhance the understanding of their spatial arrangement. (i) Delta channel: the channel deposits are primarily composed of fine-grained sandstone, with the vertical grain size showing a fining-upward trend. The thickness of the sandstone bodies generally ranges from 1 to 4 m. The GR (Gamma Ray) curve typically exhibits a medium to high-amplitude bell-shaped or box-shaped response (Fig. 15(a)). (ii) Main channel: The main channels are formed by the passage of sediment from the delta front to the semi-deep lake, predominantly filled with massive fine sandstone and argillaceous clast-rich siltstone. The thickness of the sand bodies generally exceeds 4 m. The SP curve predominantly exhibits a negative response, while the GR curve shows a high-amplitude straight bell-shaped or box-shaped response (Fig. 15(b)). (iii) Distributary channel: the distributary channels are characterized by clean massive fine-grained sandstones and massive fine-grained sandstones interspersed with mud clasts. The thickness of the sandstone bodies typically ranges from 1 to 4 m. The GR curve generally exhibits a medium to high-amplitude bell-shaped response (Fig. 15(c)). (iv) Mouth bar: the mouth bars are filled with light gray fine sandstone and siltstone; the vertical grain size shows an inverse rhythm. The GR and SP curves mainly exhibit a funnel-shaped response (Fig. 15(d)). (v) Lobe: the lobes primarily contain massive fine-grained sandstones and silty mudstone, exhibiting obvious coarsening-upward characteristics. The thickness of the sandstone bodies ranges from 0.5 to 5 m. The GR curve displays a high-amplitude funnel-shaped response (Fig. 15(e)). (vi) Levee–overbank: the levee–overbank deposits consist of planar laminated fine-grained sandstone, cross-bedded siltstone, and muddy siltstone, with some flame-like structures at the base of the main sand bodies. The thickness of the sandstone beds typically ranges from 0.5 to 2 m. Thin layers of gray-black shale are often intercalated within the succession. The GR curve typically exhibits a low-amplitude serrated bell-shaped or finger-shaped response (Fig. 15(f)).

The polynomial interpolation algorithm, specifically the convergent interpolation algorithm utilized within Petrel software (Schlumberger, Switzerland), is applied to interpolate the sand thickness derived from well logging data on the basis of the trend indicated by the fusion attribute. This approach enables the visualization and quantification of the target layer's sand thickness within the study area. The results of this prediction align with the sand thickness inferred from well logging and mirror the distribution trend of the intelligent fusion attribute, thereby providing an objective representation of the dense sand thickness in the target layer (Fig. 16(a)). With the use of predictions of sand thickness, along with well seismic data and interpretation results from single well phases, the distribution of sedimentary microfacies is illustrated within the framework of the sedimentary model (Liu et al., 2025) (Fig. 16(b)). In the shallow water area located in the southwestern part of the study region, delta deposits have developed, which are primarily composed of underwater distributary channels and estuary bars. The main channel deposits are found in the middle and upper sections of the slope, where multistage superimposed positive rhythm sand bodies achieve a cumulative thickness of 18 m. The lateral edge of the channel features channel overflow deposits, which vertically display characteristics of interlayered sand and mud, with the thicknesses of individual sand bodies generally measuring less than 2 m. In the lower portion of the slope and at the proximal end of the basin bottom zone, lake bottom fan lobes are prevalent, comprising multiple lobes distributed in a fan-shaped and continuous manner, with a total superimposed thickness exceeding 18 m. Within these lobes, narrow strip-shaped tributaries are developed, which are cut down and formed on the lobes, displaying a tree-like bifurcation along the direction of the source; the long axis direction of these tributaries is nearly parallel to the front end of the lake bottom fan. At the far end of the lake bottom, deep lake mudstone deposits primarily dominate the sedimentary landscape.

4. Discussion

4.1. Comparative analysis of the DW-DNN model and existing methods

This study selects several benchmark models (Li et al., 2025), including support vector regression (SVR), multilayer perceptron (MLP), K-nearest neighbor (KNN), channel-space dual attention network (CBAM-CNN), channel attention network (SENet), and traditional DNN, to compare their performance in predicting sand thickness via a unified dataset. The parameter configurations for each model are detailed in Table 4. The evaluation indicators include R^2, the mean absolute error (MAE), the root mean square error (RMSE), and the fusion attribute visualization results.

In terms of prediction accuracy, the DW-DNN model achieves an MAE of 1.21 on the training set and 1.25 on the test set. The corresponding RMSE values are 3.02 and 3.15, whereas the R^2 values are 0.93 and 0.92, indicating both a strong fitting ability and a strong generalization capacity (Fig. 17). The results of the fusion attributes reveal that the DW-DNN demonstrates excellent continuity and clarity of boundaries when predicting sand thickness, particularly in regions characterized by thin sand bodies, thus exhibiting high prediction accuracy and effectively capturing complex geological features. In contrast, the CBAM-CNN model yields R^2 values of 0.89 and 0.82 for the training and test sets, respectively. The MAEs recorded are 1.55 and 1.68, whereas the RMSEs are 4.26 and 4.92 (Fig. 17). Although the overall accuracy remains high, the model shows notable deficiencies in terms of the clarity of the sand body boundaries and the continuity of the fusion attributes (Fig. 18(f)), particularly in areas with thin sand bodies, resulting in significant prediction deviations. This issue primarily arises from the model's reliance on a purely data-driven dynamic weight assignment method implemented through channel attention and spatial attention mechanisms. While this approach enhances feature extraction capabilities, it suffers from poor weight adaptability because of its inadequacy in effectively

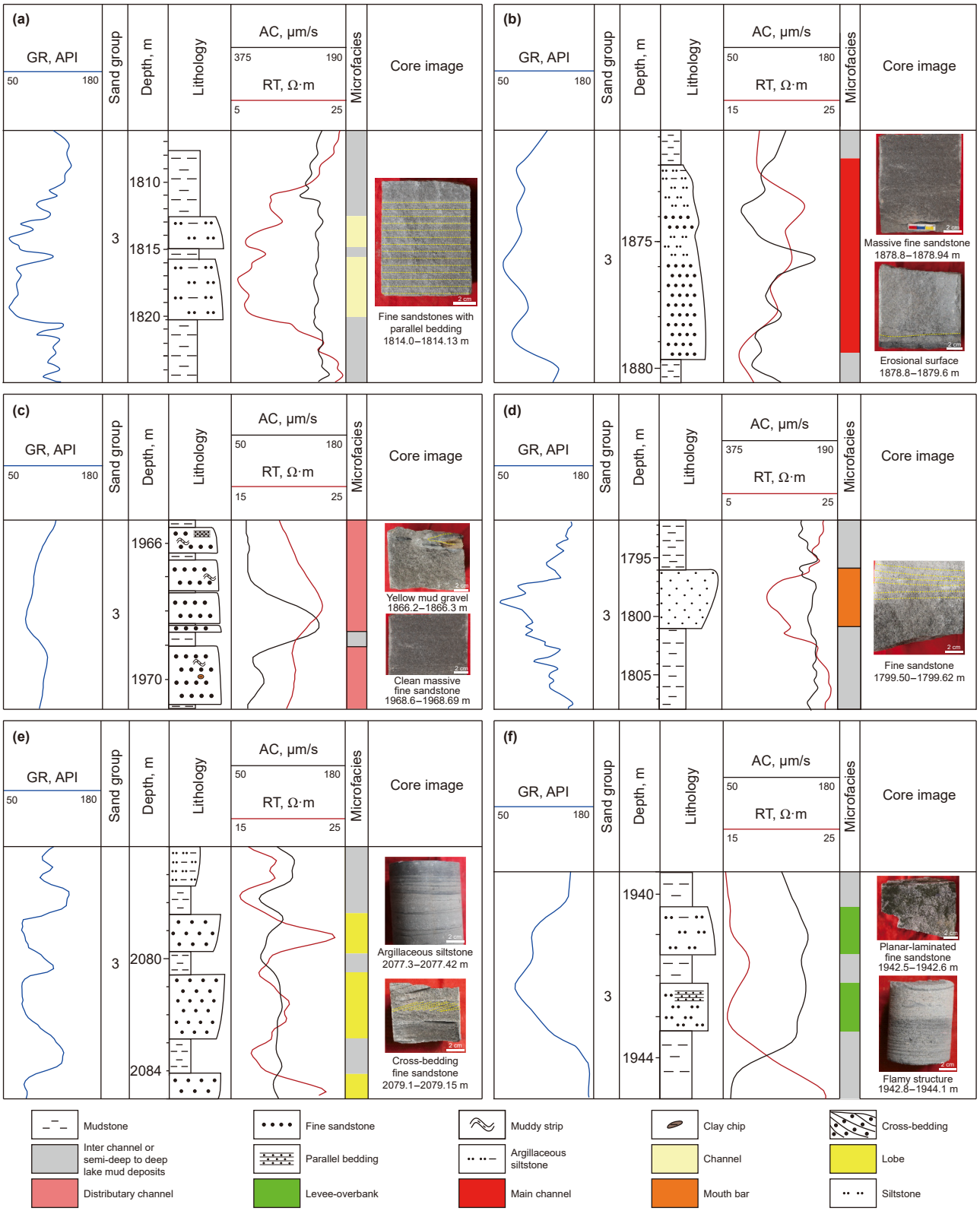

Fig. 15. Logging and core characteristics of sedimentary microfacies, **(a)** delta channel (Y48 well), **(b)** main channel (X233 well), **(c)** distributary channel (X233), **(d)** mouth bar (Y48 well), **(e)** lobe (L388 well), **(f)** levee–overbank (X233 well).

modeling changes in the sand body distribution and the relationships among seismic attributes across different frequency bands, thereby adversely affecting prediction outcomes.

SENet also employs a purely data-driven channel attention mechanism for feature weighting, yielding R^2 values of 0.91 and 0.77 for the training and test sets, respectively. The recorded MAEs

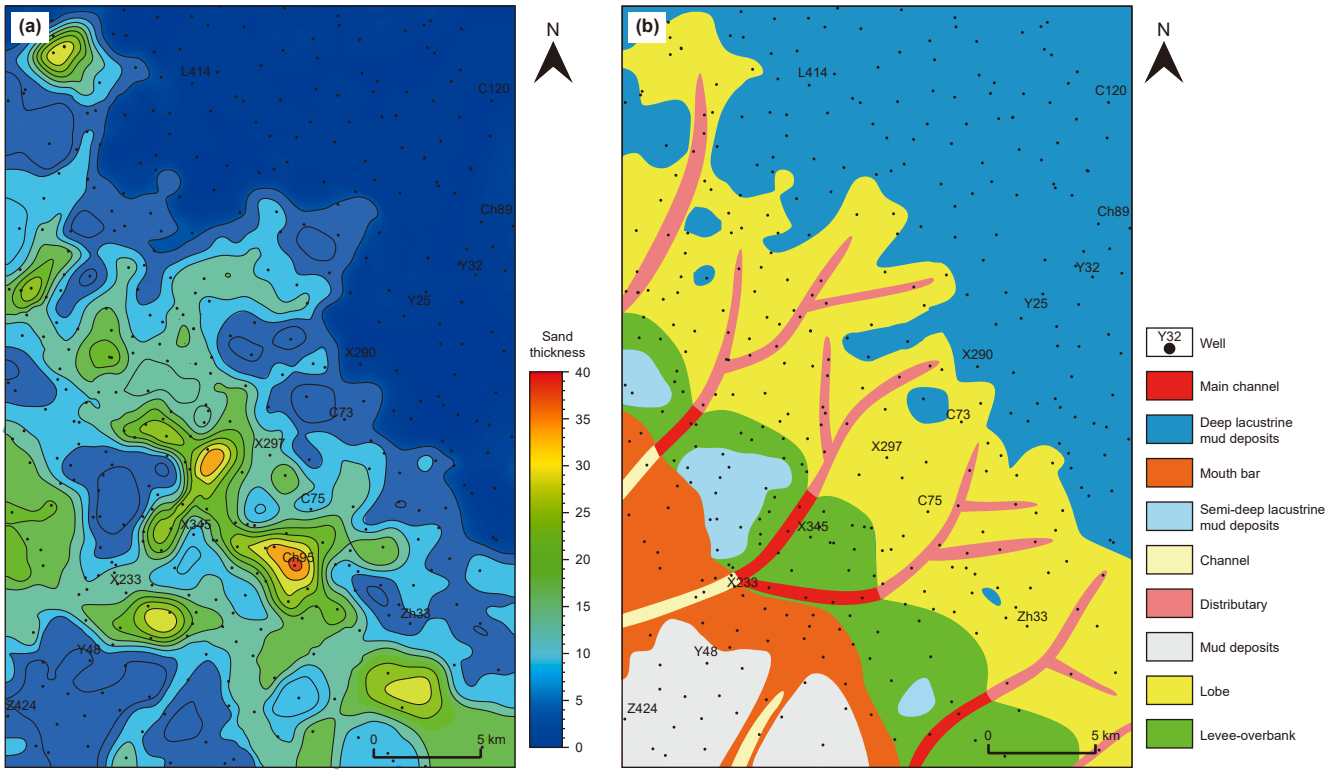

Fig. 16. Sedimentary characteristics of the third sand group, **(a)** sand body thickness distribution results based on Petrel software interpolation algorithm, **(b)** distribution characteristics of sedimentary microfacies.

Table 4
Main hyperparameters of each model.

Model	Number of layers	Activation function	Number of iterations	Regularization coefficient	Other parameter	Predicted time required, s	Relevant studies
SVR		Rbf kernel	Max_iter = −1		C = 20, epsilon = 0.1, gamma = scale, tolerance = 1e-3.	10.1211	Yin and Zhou (2005) Wang et al. (2013)
MLP	2 (50, 50)	Relu	350	L2 = 0.001	Optimizer: adam, batch size = 32.	9.4520	Xie et al. (2023)
KNN			350		n_neighbors = 7, weights = distance, metric = minkowski, p = 2, algorithm = auto.	9.1523	Song et al. (2022)
CBAM-CNN	Conv + CBAM + FC (128, 64)	Relu (conv), sigmoid (attention)	350	L2 = 0.01, Dropout = 0.3	optimizer: adam, batch size = 32, CBAM attention.	7.4210	Zhen et al. (2024)
SENet	conv + se + fc (layer = 3)	Relu	350	L2 = 0.001, dropout = 0.2	Optimizer: adam, batch size = 32, SE-block.	7.4217	Liu et al. (2015)
DNN	4 (256, 128, 128, 64)	Relu	350	Dropout = 0.2	optimizer: adam, loss = MSE, batch size = 32.	8.3046	this study
DW–DNN	4 (256, 128, 128, 64)	Relu	350	Dropout = 0.2	Optimizer: adam, loss = MSE + AVF physical constraint terms, batch size = 32.	5.3070	this study

are 1.71 and 1.82, whereas the corresponding RMSE values are 4.74 and 5.04 (Fig. 17). Despite its strong performance on the training set, the model significantly overfits the test set, leading to a marked decline in prediction accuracy, particularly in thin sand body areas (Fig. 18(e)). This suggests that SENet has limited adaptability to the substantial heterogeneity inherent in sand bodies. Furthermore, traditional models such as SVR, KNN, and MLP perform inadequately in this task (Zhao et al., 2025), primarily because of their limitations in deep feature modeling capabilities stemming from fixed weight distributions. The R^2 values for these models on the training set are 0.48, 0.44, and 0.43; on the test set, these values further decrease to 0.31, 0.23, and 0.25 (Fig. 17). The fusion attribute maps generated by these models demonstrate blurred sand body boundaries and disorganized distributions (Fig. 18(a)–(c)), which complicate the accurate reflection of the actual distribution characteristics of the sand bodies. The prediction time for DW-DNN on 10,359 entries was 5.3070 s, compared to 8–10 s for traditional DNN, SVR, and KNN. This efficiency results

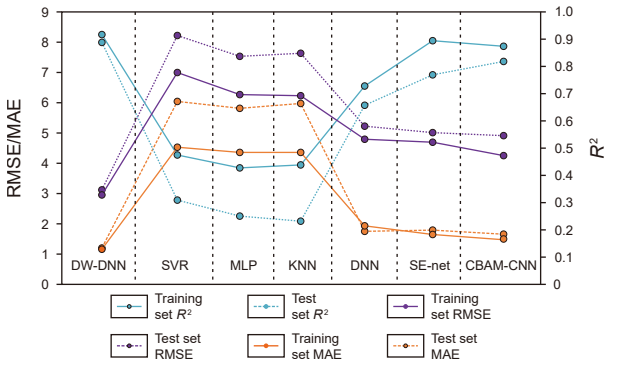

Fig. 17. Correlation indicators of different models.

from DW-DNN's self-attention mechanism, which reduces redundant computations through feature weighting. In contrast, SVR and KNN require more processing time due to the computation of support vectors or neighbor distances. DW-DNN thus demonstrates clear computational advantages while maintaining prediction accuracy, validating its practicality for large-scale data prediction tasks.

In summary, the DW-DNN model significantly enhances both the accuracy and spatial expression capabilities of sand thickness prediction (Zheng et al., 2025). By leveraging dynamic weight adjustment and multiscale information fusion, particularly in thin sand body regions and areas characterized by complex sand body distributions, it has strong robustness and adaptability. Consequently, the overall performance of the DW-DNN surpasses that of other comparative models.

4.2. Effectiveness of the adaptive weight allocation mechanism

The adaptive weighting mechanism, termed dynamic weighting (DW), enables the model to concentrate on key features by dynamically adjusting the weights assigned to the seismic attribute frequency bands at each well point. This adjustment consequently enhances the accuracy of the predictions regarding the sand thickness. To evaluate the effectiveness of this mechanism, a control experiment was designed to conduct a comprehensive comparison between the traditional DNN model and the DW-DNN model, with a focus on prediction accuracy, result visualization, and data robustness.

The experimental results indicate that the DW-DNN model significantly outperforms the traditional DNN model on the test set, achieving an R^2 value of 0.92, compared with 0.72 for the traditional DNN (Fig. 19(a)). Furthermore, the maximum prediction error was recorded at 6 m for the DW-DNN model, whereas the traditional DNN demonstrated a maximum error of 16 m. Detailed error distribution analysis revealed that, within the DW-DNN model, 60% of the well points exhibited prediction errors of less than 1 m, whereas only 4% had errors exceeding 5 m. Conversely, the traditional DNN model managed to yield only 45% of the sample errors below 1 m, with 14% surpassing the 5 m mark (Fig. 20). These findings substantiate the significant advantages of the DW-DNN in terms of prediction accuracy.

With respect to the reliability of predictions concerning the spatial distribution of sand bodies, the DW-DNN model offers more precise delineation of sand–mud boundaries and a more continuous distribution of high-value areas. In contrast, the traditional DNN model exhibits a false sand body phenomenon in the semideep to deep lake area, where the high-value region is characterized by a discrete distribution, thereby failing to accurately identify the extension direction of the waterway (Fig. 18(d)). In comparison, the DW-DNN effectively delineates the sand–mud boundary, aligning closely with well point data and clearly indicating both the extension direction of the sand body and the center of the lobe thickness, thereby providing a robust basis for constructing sedimentary phase maps. The DW mechanism considerably enhances feature resolution through the dynamic amplification of frequency band attributes that are strongly correlated with sand thickness while simultaneously suppressing interference from noise frequency bands.

To further assess the robustness of the model, a series of experiments were conducted, systematically modifying the training set ratio from 8:2 to 4:6 (Fig. 19(b)). A prediction error of less than 2 m was categorized as a correct prediction. The results from these experiments demonstrate that, at a training set ratio reduced to 50%, the DW-DNN model maintained a prediction accuracy of 0.78, significantly outperforming the CBAM-CNN (0.72), SENet (0.70), and traditional fixed weight models (such as DNN/MLP/KNN, approximately 40%). In scenarios characterized by extreme data scarcity, specifically with a training set ratio of 40%, the accuracy of the DW-DNN model was 0.66, reflecting only a 15% decrease in performance. In contrast, the accuracies of the CBAM-CNN and SENet decreased to 0.42 and 0.44, respectively, corresponding to decreases of 42% and 37%, respectively. This disparity in performance highlights the DW mechanism's capacity to establish a mapping relationship between frequency band attributes and sand thickness, even when data availability is limited, through the prior weight mechanism informed by well-point data, thereby compensating for inadequate data.

Nonetheless, the DW-DNN model has certain limitations when extremely low sample sizes are addressed. The attribute fusion results indicate that when the training set ratio is at least 50%, the DW-DNN model accurately predicts the thickness distribution of sand bodies with clear continuity and well-defined boundaries, enabling clear differentiation between thin and thick sand. However, when the training set ratio falls below 40%, particularly in deep lake areas, the model's predictions of the sand–mud boundary become increasingly indistinct. In such instances, thin sand bodies or areas devoid of sand may be erroneously classified as thick sand bodies (Fig. 21(e)). This phenomenon underscores the limitations of the DW-DNN model in managing spatial constraints under circumstances of data scarcity.

4.3. Comparison of the DW-DNN method with seismic inversion methods

Seismic inversion is one of the core technologies for reservoir prediction (Li et al., 2025; Wei et al., 2021). In this study, two mainstream seismic inversion methods—Sparse-Spike Inversion (SSI) and waveform indicator inversion (WII)—are selected as baseline comparisons to evaluate the prediction results of the DW-DNN method and the inversion methods, aiming to highlight the advantages of the proposed method in predicting sand bodies.

To ensure the comparability of the prediction results, a unified data partitioning strategy was applied, with the 317 wells in the study area randomly divided into 221 training wells and 96 blind wells in a 7:3 ratio. The SSI inversion was implemented using GeoScope (v3.8.2) commercial software, with a sparsity constraint of 0.1, a model constraint of 1, a wavelet balance of 0.3, a maximum iteration count of 1000, and L2 regularization (regularization factor of 0.01) to balance the smoothness of the inversion results and the risk of overfitting. The WII inversion was implemented using the SMI software (v4.5.2), with the waveform library constructed from the 221 training wells. The time window length employed an adaptive window strategy that automatically adjusts the matching

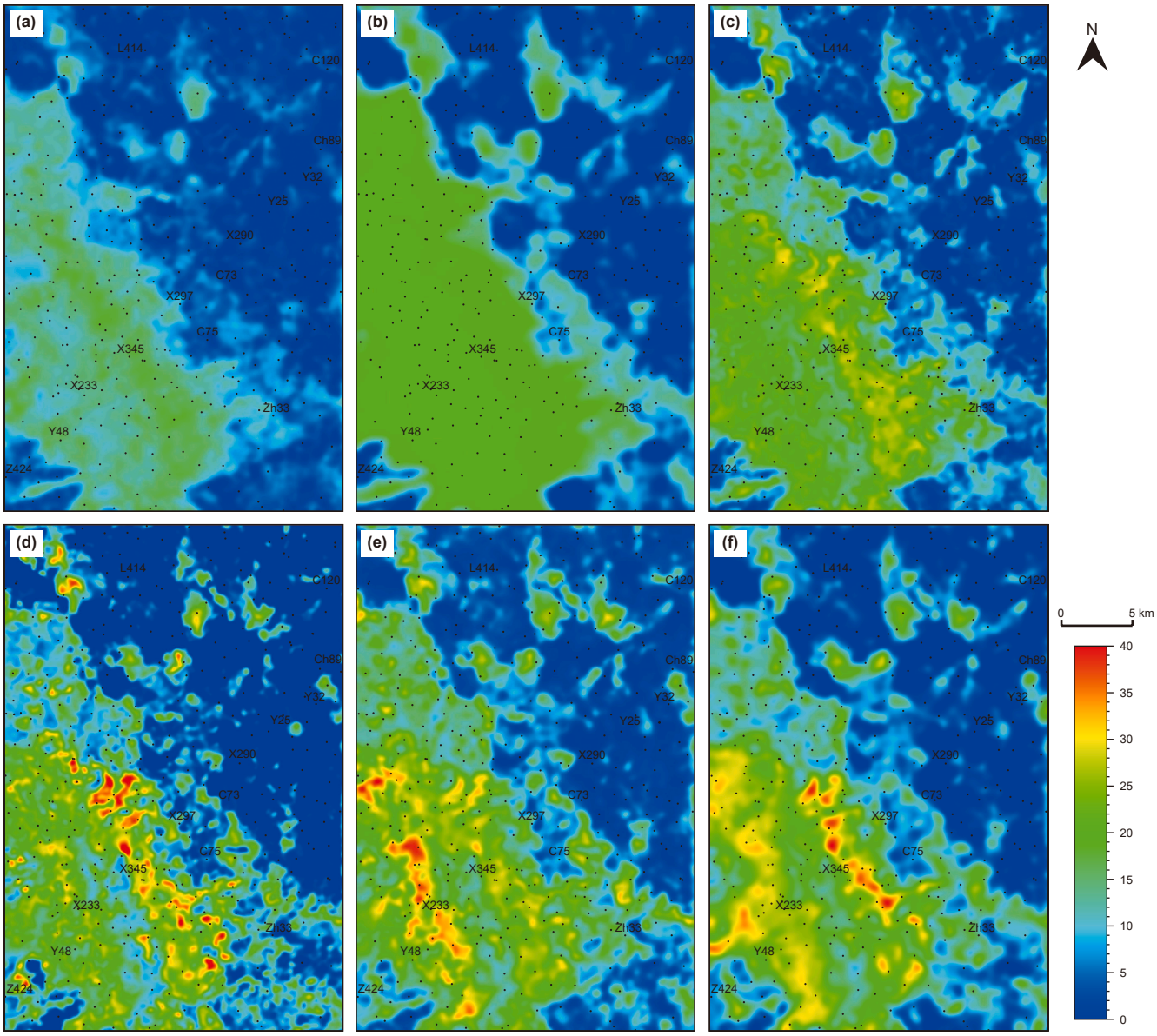

Fig. 18. Results of frequency-division seismic attributes of different methods, **(a)** the SVR method effectively outlines the boundaries of sand bodies but struggles to differentiate between thick and thin layers, **(b)** the KNN method provides distinct boundaries for sand bodies, it cannot distinguish between thick and thin layers, **(c)** the MLP method produces clear boundaries for sand bodies and successfully identifies some of the thicker sand, **(d)** the DNN method depicts the boundaries of sand bodies and allows for differentiation between thick and thin layers, although the distribution of the sand bodies is relatively dispersed, **(e)** the SENet method clearly delineates the boundaries of sand bodies, distinguishing well between thick and thin layers; however, there are instances of false sand bodies due to continuous distribution, **(f)** the CBAM-CNN method produces well-defined boundaries for sand bodies with clear differentiation between thick and thin layers, the sand body distribution is continuous, but there are areas without sand bodies that can appear as false sand.

range according to the dynamic variations in well data, thus enhancing the ability to characterize lateral heterogeneity.

The experimental results indicate that, based on the SSI inversion, the sand body profile shows clear vertical differentiation with good lateral continuity (Fig. 22(b)). Overall, the predicted sand body thickness is thicker than the sand thickness from wells, with higher prediction accuracy in areas with thick or multiple overlain sand bodies. For example, in the region marked by the red circle in Fig. 22(b) (blind well X327), which represents a typical sand-shale interlayer, the inversion results show high values, roughly indicating the location of the sand body. However, it is difficult to distinguish the thin shale layers within it. In areas with a single thin sand body, the predicted thickness is significantly higher than the sand thickness from wells. Based on WII inversion, the sand body profile not only shows clear vertical differentiation but also a more defined lateral distribution of the sand body, with the spatial distribution and stacking relationships being well presented (Fig. 22(c)). The predicted sand body thickness is in good agreement with the well data, especially in the sand-shale interlayer and thick sand body regions. However, in areas with a single thin sand body, issues such as unrecognized or overly thick predictions arise. Regarding prediction accuracy, the R^2 of WII inversion for predicting the sand body thickness based on blind well data is 0.79 (Fig. 23(b)), which shows good overall prediction performance, with the error primarily concentrated in wells with a sand body thickness of less than 15 m. In contrast, the R^2 of SSI inversion is

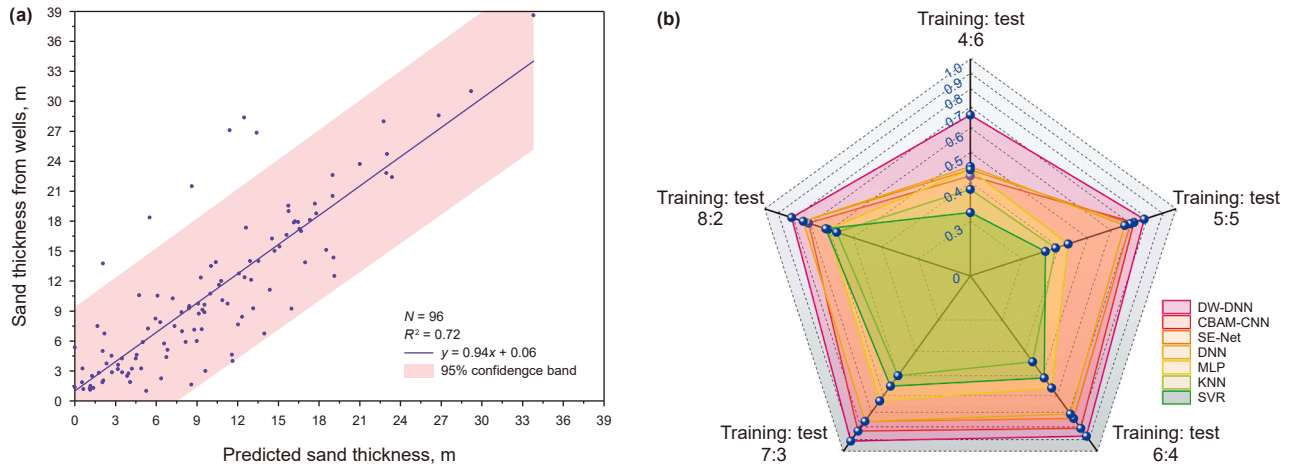

Fig. 19. Model prediction effect on the test set, **(a)** comparison of the DW-DNN model predictions and actual values on the test set (R^2 = 0.72), **(b)** prediction accuracy of the models under different data split ratios.

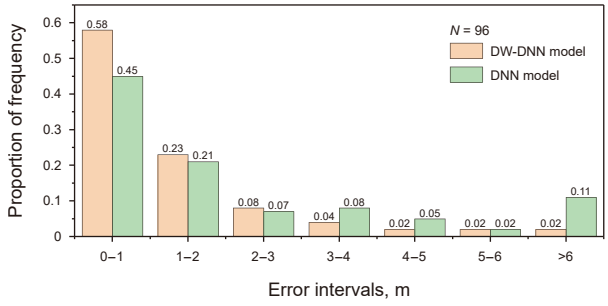

Fig. 20. Distribution of differences between the predictions and actual values for different models on the test set.

0.67 (Fig. 23(a)), with errors mainly concentrated in wells with a sand body thickness of less than 10 m, though its performance is relatively better for sand bodies thicker than 10 m.

In conclusion, under the same data conditions, the DW-DNN method proposed in this study demonstrates superior prediction accuracy in blind well prediction, with an R^2 of 0.92, which is higher than that of Sparse-Spike Inversion (R^2 = 0.67) and Waveform Indicator Inversion (R^2 = 0.79). All three methods show good prediction ability for sand bodies thicker than 10 m, but the seismic inversion methods exhibit more distinct advantages in characterizing the spatial distribution and stacking relationships of sand bodies. However, in predicting thin sand bodies less than 10 m, traditional inversion methods can roughly reflect the vertical distribution but suffer from significant prediction errors in terms of sand body thickness. In contrast, the DW-DNN method is more accurate in characterizing the planar thickness distribution of thin sand bodies, though it still cannot explain the internal distribution patterns of the sand bodies. Therefore, future research could further explore a combined strategy that integrates the strengths of DW-DNN in planar thickness prediction and seismic inversion methods in vertical continuity, thereby improving the overall accuracy of sand body prediction.

4.4. Applicable conditions and prospects of the DW-DNN method

The DW-DNN method proposed in this study is applicable to most sandstone reservoirs, particularly under the following conditions: First, the method relies on an adequate quantity of well data and specific seismic frequency bands to construct the prior knowledge necessary for machine learning. However, when the study area is predominantly composed of thick or thin sand bodies, the construction of prior knowledge may exhibit inherent biases, especially when the training set lacks specific features. This can lead to a decline in model performance. Therefore, the distribution and density of wells are critical factors affecting the method's performance in practical applications. A well network needs to be relatively evenly distributed to ensure data representativeness, especially in complex geological environments with shallow or thin sand bodies. For example, in the Xi 233 area, which spans 832 km^2 and contains 317 wells for sand body prediction, the optimal ratio of training to testing sets is 7:3, resulting in a well density of 0.27 (density = number of wells/area), which yields the best model performance. As the size of the training set is gradually reduced, a decline in model performance is observed. Specifically, when the well density decreases to 0.19 (with the training-to-testing ratio adjusted to 5:5), the method still effectively predicts the sand body distribution, although there is some deviation in the prediction of sand thickness. However, when the training-to-testing ratio is further reduced to 4:6 (resulting in a well density of 0.15), the method nearly fails in delineating the boundaries of the sand body. Thus, the well density and distribution within the study area are crucial to the effectiveness of the method. Moreover, the DW-DNN method is particularly well-suited for sedimentary basins with distinct sand body structures, such as river channels, deltas, and other regions characterized by clear sedimentary features. In these areas, where sand body thickness variations are more pronounced and the relationship between seismic attributes and sand body characteristics is more straightforward, the model can be effectively trained and applied. In contrast, the method's performance may face challenges in complex geological environments, especially those affected by significant stratigraphic interference or noise. Future research could explore seismic data optimization techniques, including denoising, attribute enhancement, and data fusion, to further improve the method's noise resistance and adaptability.

Although the DW-DNN method has demonstrated significant advantages in predicting sand thickness, particularly in identifying thin sand bodies, characterizing boundaries, and exhibiting robustness in scenarios characterized by limited data, it nonetheless possesses certain limitations that warrant further optimization and expansion in future research.

First, the spatial constraint capability of the DW-DNN model diminishes under conditions of extreme data scarcity, specifically

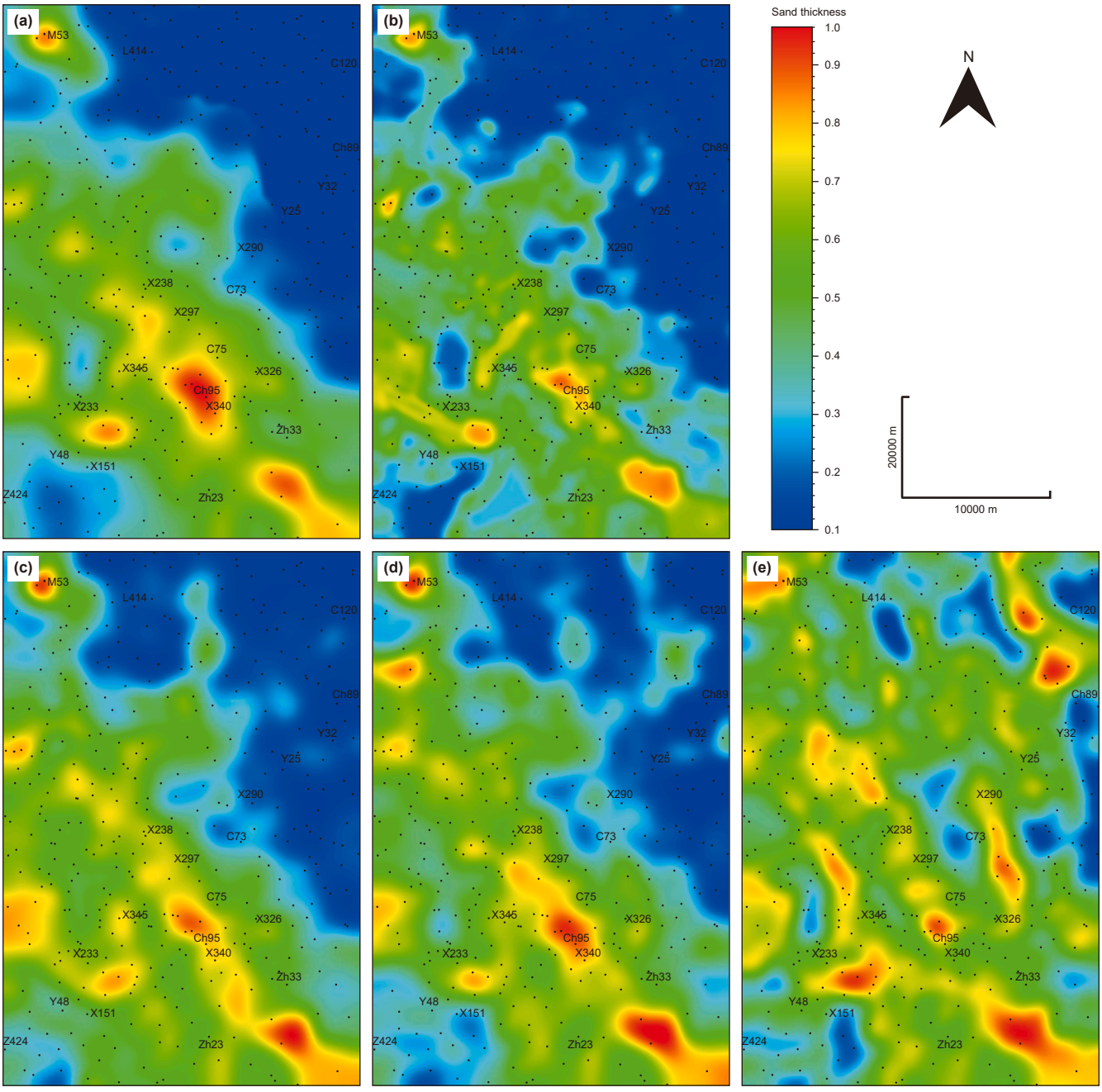

Fig. 21. Fusion attribute results of the DW-DNN model under different data split ratios, **(a)** 80% training set and 20% test set, **(b)** 70% training set and 30% test set, **(c)** 60% training set and 40% test set, **(d)** 50% training set and 50% test set, and **(e)** 40% training set and 60% test set.

when the training set comprises less than 40% of the required samples. The experimental results indicate that, in instances of insufficient training samples, the model is prone to issues such as blurred sand–mud boundaries and the misclassification of thin sand or sandless areas as thick sand bodies in complex geological environments, such as deep lakes. This phenomenon primarily arises because the adaptive weight mechanism, which is informed by well points, faces challenges in accurately establishing the mapping relationship between seismic frequency band attributes and sand thickness in the absence of adequate prior information. Consequently, this results in a marked decline in local prediction accuracy. Therefore, enhancing the model's ability to perceive spatial distribution characteristics under extremely low sample sizes represents a crucial avenue for future enhancements.

Second, while the current DW-DNN model bolsters key frequency band attributes through a dynamic weight mechanism, considerable potential remains for improvement in multiscale feature fusion and cross-band collaborative modeling. Current methodologies are predominantly reliant on weight adjustments dictated by single-point well data, neglecting to fully account for the global correlations among seismic attributes across different frequency bands, as well as their collective response to sand body heterogeneity. The introduction of a more sophisticated frequency band interaction modeling mechanism, such as an attention-based cross-band feature fusion strategy, may enhance the model's capacity to characterize complex geological structures.

Finally, from an engineering application standpoint, optimization of the computational efficiency of the DW-DNN model

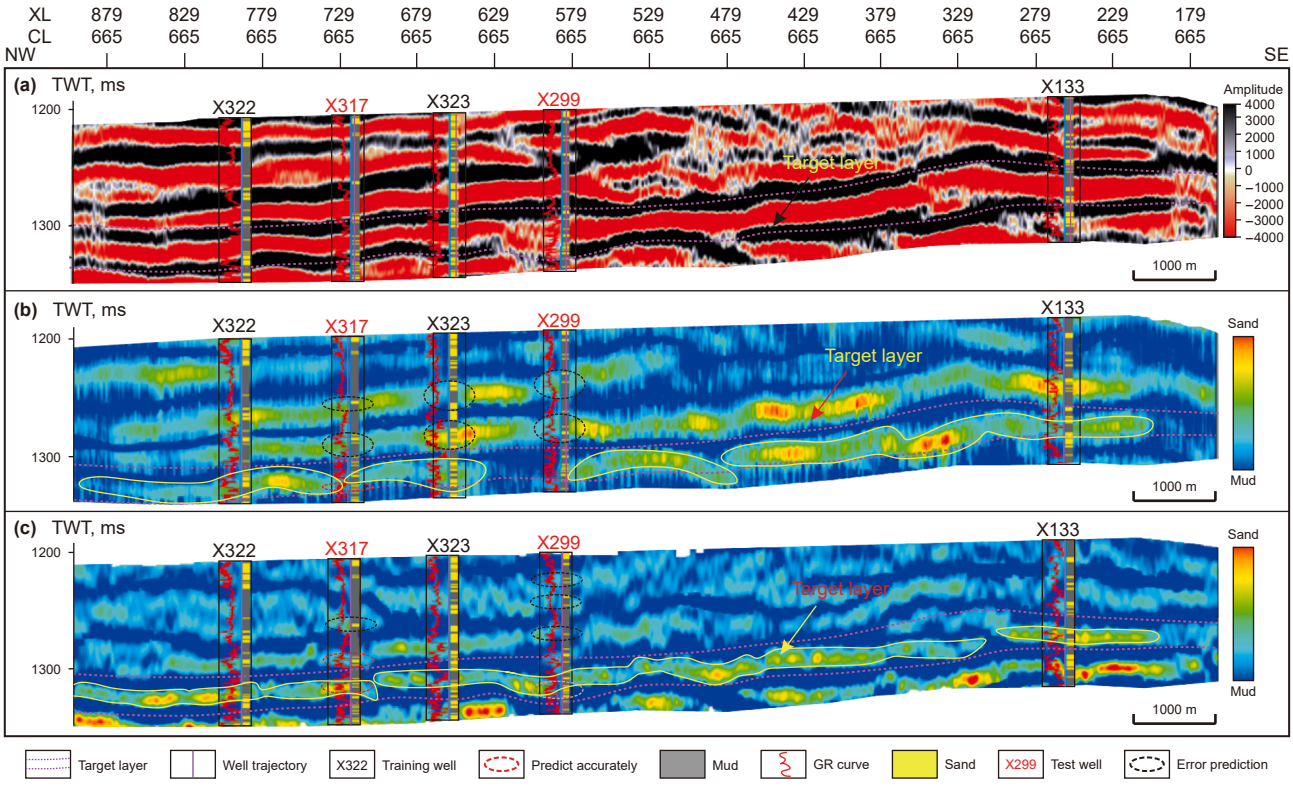

Fig. 22. Seismic inversion profiles using different methods, **(a)** original seismic profile, **(b)** sparse-spike inversion profile, **(c)** waveform indicator inversion profile (profile location shown in Fig. 6(c) A–A').

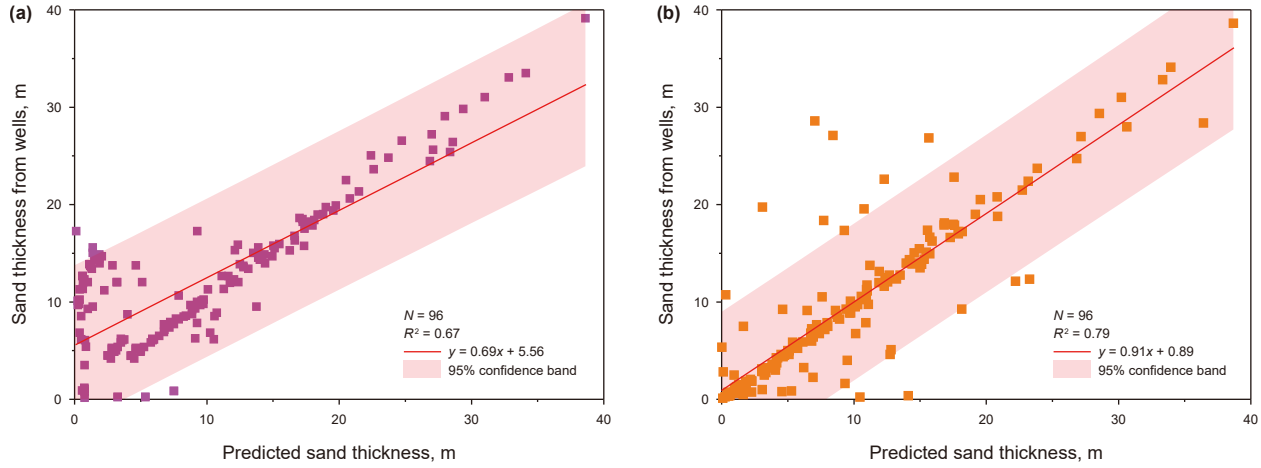

Fig. 23. Prediction accuracy of sand thickness by different seismic inversion methods, **(a)** SSI inversion predictions and actual values on the test set ($R^2 = 0.67$), **(b)** WII inversion predictions and actual values on the test set ($R^2 = 0.79$).

remains necessary. As the depth of the network and the number of frequency bands increase, both the training and inference times are extended, potentially constraining real-time deployment in large-scale, three-dimensional seismic data contexts. To address this issue, the exploration of lightweight network architecture designs, parallel computing acceleration, or model compression technologies may be warranted to achieve a balance between high precision and high efficiency.

In conclusion, the DW-DNN method demonstrates considerable potential for predicting sand body thickness, especially in regions characterized by high well density, appropriate frequency selection, and clearly defined sedimentary features. Nevertheless, the method's robustness, multi-frequency band collaborative modeling capability, noise resistance, and computational efficiency require further optimization, particularly in data-scarce and complex geological environments. Future research should prioritize integrating geological prior knowledge, multi-source data fusion, the development of innovative neural network architectures, and the exploration of synergies with geophysical inversion methods. These efforts will help to better understand sand body distribution patterns and stacking configurations, providing a more reliable geological basis for accurate reservoir prediction and optimal well placement.

5. Conclusions

The DW-DNN model introduced in this study effectively enhances the prediction accuracy of the sand thickness by integrating physical constraints with deep learning technologies. The principal conclusions are as follows:

(1) This study proposes a frequency-decomposed attribute fusion method that uses adaptive weights. This approach leverages the AVF-tuning thickness difference to construct a geological prior constraint matrix while also incorporating an attention mechanism to dynamically optimize the weights of frequency-decomposed seismic attributes. By accounting for the mapping relationship between seismic attributes across different frequency bands and sand thickness, this method facilitates the identification of regions where thin sand bodies present high-frequency attribute responses. Conversely, areas characterized by thick sand bodies predominantly utilize low-frequency attributes, thereby increasing the prediction accuracy of multiattribute fusion and addressing the limitations associated with traditional fixed-weight fusion techniques.

(2) The DW-DNN model demonstrates notable accuracy in predicting sand thickness, achieving a prediction accuracy R^2 value of 0.92, which represents a 24.3% improvement over conventional deep neural network (DNN) methods. The average prediction error at the well point locations is minimal, measuring only 2 m for sand thicknesses ranging from 0 to 3 m. Notably, as the sand thickness increases, the prediction error exhibits a gradient that decreases progressively; in thick sand body areas, the average error further decreases to 0.68 m. Furthermore, 93% of the well points experienced a prediction error of less than 3 m. Compared with existing models such as MLP, SVR, KNN, CBAM-CNN, and SENet, the DW-DNN model consistently provides superior evaluation metrics. Additionally, even when limited well data are available, the prediction accuracy of the DW-DNN model for untested wells surpasses that of alternative models, yielding a more continuous distribution of sand body predictions and more precise boundaries, further underscoring its efficacy in scenarios with sparse well data.

(3) In practical applications involving the third sand group of the third section of the Yanchang Formation in the Xi 233 area of the Ordos Basin, the DW-DNN model is capable of accurately predicting the sand body boundaries of various depositional features, including estuary bars, river channels, channel overflows, main channels, branch channels, and lobes. The model clearly delineates the extension direction of the channel, the center of the lobe thickness, and the characteristics of the secondary fan shape. Developed delta deposits characterize the near-provenance area, whereas the far-provenance area exhibits a gradual transition to fan-shaped lobe deposits. The branch channel distinctly cuts across the lobe, and the model's prediction results align closely with the spatial distribution patterns of the actual sedimentary facies.

CRediT authorship contribution statement

Hong-Li Wu: Writing – original draft, Visualization, Validation, Software, Resources, Project administration, Methodology, Investigation, Funding acquisition, Formal analysis, Data curation, Conceptualization. **Sheng-He Wu:** Writing – review & editing, Supervision, Funding acquisition. **Zhen-Hua Xu:** Writing – review & editing, Supervision, Funding acquisition. **Ming-Cheng Liu:** Writing – review & editing, Visualization, Validation. **De-Gang Wu:** Writing – review & editing, Visualization, Validation. **Bo Yang:** Visualization, Methodology, Data curation. **Zi-Shi Xie:** Visualization, Software, Investigation. **Yu Tang:** Methodology, Data curation. **Xiao-Long Wan:** Resources, Data curation. **Xin-Ping Zhou:** Resources, Data curation.

Declaration of competing interest

The authors declare that they have no known competing financial interests or personal relationships that could have appeared to influence the work reported in this paper.

Acknowledgements

This study is funded by the Science Foundation of China University of Petroleum (Beijing) (Grant No. 2462025BJRC005), Strategic Cooperation Technology Projects of China National Petroleum Corporation (CNPC) and China University of Petroleum (Grant No. ZLZX2020-02), Major Science and Technology Project of Changqing Oilfield (Grant No. 2023DZZ04), and China University of Petroleum (Grant No. 2462023YJRC034), and the National Natural Science Foundation of China (Grant No. 42202178, 42272110).

References

Ali, M., Changxingyue, H., Wei, N., et al., 2025. Optimizing seismic-based reservoir property prediction: A synthetic data-driven approach using convolutional neural networks and transfer learning with real data integration. Artif. Intell. Rev. 58, 31. https://doi.org/10.1007/s10462-024-11030-8.

Bahdanau, D., Cho, K., Bengio, Y., 2014. Neural machine translation by jointly learning to align and translate. Comp. Sci. https://doi.org/10.48550/arXiv.1409.0473.

Bitrus, P.R., Iacopini, D., Bond, C.E., 2016. Defining the 3D geometry of thin shale units in the sleipner reservoir using seismic attributes. Mar. Petrol. Geol. 78, 405–425. https://doi.org/10.1016/j.marpetgeo.2016.09.020.

Cui, Z.S., Chen, Q.Y., Luo, J., et al., 2024. Characterizing subsurface structures from hard and soft data with multiple-condition fusion neural network. Water Resour. Res. 60 (11), e2024WR038170. https://doi.org/10.1029/2024WR038170.

Chopra, S., Marfurt, K.J., 2005. Seismic attributes — a historical perspective. Geophysics 70 (5), 3–28. https://doi.org/10.1190/1.2098670.

Chen, D., Zhang, W., Li, C.H., 2025. Randomly generating realistic calcareous sand for directional seepage simulation using deep convolutional generative adversarial networks. J. Rock Mech. Geotech. Eng. https://doi.org/10.1016/j.jrmge.2025.01.055.

Dong, Z.T., Tian, S.S., Xue, H.T., et al., 2024. Analysis of pore types in lower Cretaceous Qingshankou shale influenced by electric heating. Energy Fuels 38 (21), 20577–20590. https://doi.org/10.1021/acs.energyfuels.4c03783.

Dorrington, K.P., Link, C.A., 2004. Genetic-algorithm/neural-network approach to seismic attribute selection for well-log prediction. Geophysics 69 (1), 212–221. https://doi.org/10.1190/1.1649389.

Fu, L., Guo, J.X., Shen, W.S., et al., 2024. Geophysical evidence of the collisional suture zone in the prydz bay, east Antarctica. Geophys. Res. Lett. 51 (2), e2023GL106229. https://doi.org/10.1029/2023GL106229.

Gan, B.C., Li, Z.D., Huo, W.X., et al., 2025. Phase transitions of CH_4 hydrates in mud-bearing sediments with oceanic laminar distribution: Mechanical response and stabilization-type evolution. Fuel 380, 133185. https://doi.org/10.1016/j.fuel.2024.133185.

He, K.M., Zhang, X.Y., Ren, S.Q., et al., 2016. Deep residual learning for image recognition. 2016 IEEE Conference on Computer Vision and Pattern Recognition (CVPR), Las Vegas, NV, USA, pp. 770–778. https://doi.org/10.1109/CVPR.2016.90.

Jeffrey, H., 2018. Ian goodfellow, Yoshua Bengio, and Aaron Courville: Deep learning. Genet. Program. Evolvable Mach. 19 (1–2), 305–307. https://doi.org/10.1007/s10710-017-9314-z.

Jia, C.Z., Pang, X.Q., Song, Y., 2023. Whole petroleum system and ordered distribution pattern of conventional and unconventional oil and gas reservoirs. Pet. Sci. 20 (1), 1–19. https://doi.org/10.1016/j.petsci.2022.12.012.

LeCun, Y., Bengio, Y., Hinton, G., 2015. Deep learning. Nature 521 (7553), 436–444. https://doi.org/10.1038/nature14539.

Li, J.B., Hu, Z.W., Cui, J.Z., et al., 2024. Efficient GPU-accelerated seismic analysis strategy and scenario simulation for large-scale nuclear structure cluster-soil interaction over ten million DOFs. Comput. Geotech. 174, 106583. https://doi.org/10.1016/j.compgeo.2024.106583.

Li, H., Sun, L.P., Wang, X.C., et al., 2025. Multivariate information fusion modeling method and its application in seismic pre-stack inversion of shallow gas reservoir. Gas Sci. Eng. 139. https://doi.org/10.1016/j.jgsce.2025.205615.
Li, X.B., Liu, H.Q., Yang, W.W., et al., 2023. A lacustrine basin driven by extreme events of alternate dry-wet climatic cycles: Evidence from outcrops of Yanchang Formation in Upper Triassic, Ordos Basin. Earth Sci. 48 (1), 293–316. https://doi.org/10.3799/dqkx.2022.463 (in Chinese).
Li, W., Yue, D.L., Wang, W.F., et al., 2019a. Fusing multiple frequency-decomposed seismic attributes with machine learning for thickness prediction and sedimentary facies interpretation in fluvial reservoirs. J. Petrol. Sci. Eng. 177, 1087–1102. https://doi.org/10.1016/j.petrol.2019.03.017.
Li, W., Yue, D.L., Hu, G.Y., et al., 2017. Frequency-segmented seismic attribute optimization and sandbody distribution prediction: An example in North Block, Qinghuangdao 32-6 Oilfield. Oil Geophys. Prospect. 52 (1), 121–130. https://doi.org/10.13810/j.cnki.issn.1000-7210.2017.01.017 (in Chinese).
Li, W., Yue, D.L., Wu, S.H., et al., 2019b. Characterizing meander belts and point bars in fluvial reservoirs by combining spectral decomposition and genetic inversion. Mar. Petrol. Geol. 105, 168–184. https://doi.org/10.1016/j.marpetgeo.2019.04.015.
Liu, F., Zhu, X.M., Li, Y., et al., 2015. Sedimentary characteristics and facies model of gravity flow deposits of Late Triassic Yanchang Formation in Southwestern Ordos Basin, NW China. Petrol. Explor. Dev. 42 (5), 577–588. https://doi.org/10.11698/PED.2015.05.04 (in Chinese).
Liu, Z.B., Zhu, J.M., Tian, B., et al., 2024a. A novel seismic inversion method based on multiple attributes and machine learning for hydrocarbon reservoir prediction in Bohai Bay Basin, Eastern China. Front. Earth Sci. 12. https://doi.org/10.3389/feart.2024.1498164.
Liang, X.W., Xian, B.Z., Feng, S.B., et al., 2022. Architecture and main controls of gravity-flow sandbodies in Chang 7 Member, Longdong Area, Ordos Basin. Acta Sedimentol. Sin. 40 (3), 641–652. https://doi.org/10.14027/j.issn.1000-0550.2021.017 (in Chinese).
Liu, L., Li, W., Du, Y.S., et al., 2024b. Reservoir prediction method of fusing frequency-decomposed seismic attributes using Stacking ensemble learning. Oil Geophys. Prospect. 59 (1), 12–22. https://doi.org/10.13810/j.cnki.issn.1000-7210.2024.01.002.
Liu, Y.Y., Ma, X.H., Zhang, X.W., et al., 2021. A deep-learning-based prediction method of the estimated ultimate recovery (EUR) of shale gas wells. Pet. Sci. 18 (5), 1450–1464. https://doi.org/10.1016/j.petsci.2021.08.007.
Liu, H.Q., Yuan, J.Y., Li, X.B., et al., 2007. Lake basin evolution of Ordos Basin during Middle-Late Triassic and its origin analysis. Lithologic Reserv. 19 (1), 52–56. https://doi.org/10.3969/j.issn.1673-8926.2007.01.009 (in Chinese).
Liu, M.C., Wu, S.H., Yue, D.L., et al., 2025. Palaeogeomorphological control on the depositional architecture of lacustrine gravity-flow deposits in a depression lacustrine basin: A case study of the Triassic Yanchang Formation, southern Ordos Basin. China. J. Palaeogeogr. 14 (2), 476–500. https://doi.org/10.1016/j.jop.2025.01.003.
Lyu, Q.Q., Fu, J.H., Luo, S.S., et al., 2022. Sedimentary characteristics and model of gravity flow channel - lobe complex in a depression lake basin: A case study of Chang 7 Member of Triassic Yanchang Formation in southwestern Ordos Basin, NW China. Petrol. Explor. Dev. 49 (6), 1323–1338. https://doi.org/10.11698/PED.20220295.
Lyu, D.W., Zhao, Y.T., Steel, R.J., et al., 2025. Massive organic carbon burial in the North China Basin is a main contributor to peak late Paleozoic Ice Age in early Asselian. Earth Planet Sci. Lett. 661, 119370. https://doi.org/10.1016/j.epsl.2025.119370.
Ma, Y.Z., Gomez, E., Luneau, B., et al., 2011. Integrated Reservoir Modeling of a Pinedale tight-gas Reservoir in the Greater Green River Basin, vol. 96. American Association of Petroleum Geologists, Wyoming, pp. 89–106. https://doi.org/10.1306/13301409M963458.
Niu, Q.H., Wang, J., He, J.B., et al., 2025. Inversion and optimization of CO_2+O_2 in situ leaching of blasting-stimulated sandstone-type uranium deposits. Phys. Fluids 37 (3), 036639. https://doi.org/10.1063/5.0264620.
Partyka, G., Gridley, J., Lopez, J., 1999. Interpretational applications of spectral decomposition in reservoir characterization. Lead. Edge 18 (3), 353–360. https://doi.org/10.1190/1.1438295.
Sang, K.H., Yin, X.Y., Zhang, F.C., 2021. Machine learning seismic reservoir prediction method based on virtual sample generation. Pet. Sci. 18 (6), 1662–1674. https://doi.org/10.1016/j.petsci.2021.09.034.
Saggaf, M.M., Nebrija, E.L., 2003. A fuzzy logic approach for the estimation of facies from wire-line logs. AAPG Bull. 87 (7), 1223–1240. https://doi.org/10.1306/02260301019.
Sinha, S., Routh, P.S., Anno, P.D., et al., 2005. Spectral decomposition of seismic data with continuouswavelet transform. Geophysics 70 (6), 19–25. https://doi.org/10.1190/1.2127113.
Song, L., Yin, X.Y., Zong, Z.Y., et al., 2022. Two-stage semi-supervised learning inversion for reservoir physical parameters. J. Petrol. Sci. Eng. 216. https://doi.org/10.1016/j.petrol.2022.110794.
Stark, T., 2006. Visualization techniques for enhancing stratigraphic inferences from 3D seismic data volumes. First Break 24 (4), 75–85. https://doi.org/10.3997/1365-2397.24.1094.26926.
Sun, H.B., Wang, Y.Y., Jia, L.S., et al., 2024. Theoretical and numerical methods for predicting the structural stiffness of unbonded flexible riser for deep-sea mining under axial tension and internal pressure. Ocean. Eng 310 (1), 118672. https://doi.org/10.1016/j.oceaneng.2024.118672.
VÁCLAV, B., 2023. Kirchhoff pre-stack depth scalar migration of complete wave field using the prevailing-frequency approximation of the coupling ray theory. J. Seismic Explor. 32 (2), 105–129. https://doi.org/10.1111/1365-2478.13051.
Vaswani, A., Shazeer, N.M., Parmar, N., et al., 2017. Attention is all you need. neural information processing systems. Proceedings of the 31st International Conference on Neural Information Processing Systems 6000–6010. https://doi.org/10.48550/arXiv.1706.03762.
Wang, K.Y., Xu, Q.Y., Zhang, G.F., et al., 2013. Summary of seismic attribute analysis. Prog. Geophys. 28 (2), 815–823. https://doi.org/10.6038/pg20130231.
Wang, J., Guan, D.Y., Huang, X.B., et al., 2025. Integrated SOM multi-attribute optimization and seismic waveform inversion for thin sand body characterization: A case study of the Paleogene Lower E_3d_2 Sub-Member in the HHK depression, Bohai Bay Basin. Appl. Sci. 15 (9), 5134. https://doi.org/10.3390/app15095134.
Wang, K.Y., Cao, J., Ye, J.H., et al., 2024. Discrete element analysis of geosynthetic reinforced pile-supported embankments. Constr. Build. Mater. 449, 138448. https://doi.org/10.1016/j.conbuildmat.2024.138448.
Wei, M., Li, S.J., Shi, X.P., et al., 2021. Application of a seismic motion inversion method for thin reservoir prediction in the Zhuang-3 block of the Central Junggar Basin. Geophys. Prospect. Pet. 60 (4), 643–651. https://doi.org/10.3969/j.issn.1000-1441.2021.04.013.
Widess, M.B., 1973. How thin is a thin bed? Society of Exploration Geophysicists 38 (6), 1176–1180. https://doi.org/10.1190/1.1440403.
Xie, P.F., Hou, J.G., Duan, D.P., et al., 2023. A novel genetic inversion workflow based on spectral decomposition and convolutional neural networks for sand prediction in Xihu Sag of East China Sea. Geoenergy Sci. Eng. 12. https://doi.org/10.1016/j.geoen.2023.212331.
Xu, D.S., Zhang, Z.J., Qin, Y., et al., 2022. Effect of particle size distribution on dynamic properties of cemented coral sand under SHPB impact loading. Soil Dynam. Earthq. Eng. 162, 107438. https://doi.org/10.1016/j.soildyn.2022.107438.
Yang, J.J., Li, K.Q., Zhang, D.S., 1992. China petroleum Geology Volume 12 Changqing Oilfield. Petroleum Industry Press, Beijing, pp. 47–55 (in Chinese).
Yin, Z.J., Li, Y.Z., Zhang, J.M., et al., 2024. Fine characterization of braided river reservoir architecture with sparse well patterns based on intelligent fusion of multiple seismic attributes: A case study of the Guantao Formation from C-6 oilfield, Bohai Bay Basin. Acta Sedimentol. Sin. 1–15. https://doi.org/10.14027/j.issn.1000-0550.2024.022 (in Chinese).
Yin, X.Y., Zhou, J.Y., 2005. Summary of optimum methods of seismic attributes. Oil Geophys. Prospect. 40 (4), 482–489.
Yu, H., Zhao, Z.Y., Taleghani, A.D., et al., 2024. Modeling thermal-induced wellhead growth through the lifecycle of a well. Geoenergy Sci. Eng. 241, 213098. https://doi.org/10.1016/j.geoen.2024.213098.
Yue, D.L., Li, W., Du, Y.S., et al., 2022. Review on optimization and fusion of seismic attributes for fluvial reservoir characterization. Earth Sci. 47 (11), 3929–3943. https://doi.org/10.3799/dqkx.2022.221 (in Chinese).
Zhang, K., Lin, N.T., Yang, J.Q., et al., 2022. Predicting gas-bearing distribution using DNN based on multi-component seismic data: Quality evaluationusing structural and fracture factors. Pet. Sci. 19 (4), 1566–1581. https://doi.org/10.1016/j.petsci.2022.02.008.
Zeng, H.L., 2017. Thickness imaging for high-resolution stratigraphic interpretation by linear combination and color blending of multiple-frequency panels. Interpretation 5 (3), 411–422. https://doi.org/10.1190/INT-2017-0034.1.
Zhang, H., Bao, X.Y., Zhao, H., et al., 2025. High-precision deblending of 3-D simultaneous source data based on prior information constraint. IEEE geoscience and remote sensing letters 22, 1–5. https://doi.org/10.1109/LGRS.2025.3526972.
Zhen, Y., Zhang, A., Zhao, X.M., et al., 2024. Prediction of deep low permeability sandstone seismic reservoir based on CBAM-CNN. Geoenergy Sci. Eng. 242. https://doi.org/10.1016/j.geoen.2024.213241.
Zhao, D.F., Yang, N.X., Xiong, J.L., et al., 2023. Model-constrained and data-driven double-supervision acoustic impedance inversion. Pet. Sci. 20 (5), 2809–2821. https://doi.org/10.1016/j.petsci.2023.03.019.
Zhang, L., Yuan, X.C., Luo, L., et al., 2024. Seepage characteristics of broken carbonaceous shale under cyclic loading and unloading conditions. Energy Fuels 38 (2), 1192–1203. https://doi.org/10.1021/acs.energyfuels.3c04160.
Zhao, H.G., 2004. Structural Characteristics and the Evolution in Western Ordos Basin. Doctoral dissertation of Northwest University, pp. 1–143 (in Chinese).
Zeng, H.L., Backus, M.M., 2005. Interpretive advantages of 90°-phase wavelets: part 1 — modeling. Geophysics 70 (3), C7–C15. https://doi.org/10.1190/1.1925740.
Zeng, H.L., 2010. Geologic significance of anomalous instantaneous frequency. Geophysics 75 (3), 23–30. https://doi.org/10.1190/1.3427638.
Zhu, X.M., Deng, X.Q., Liu, Z.L., et al., 2013. Sedimentary characteristics and model of shallow braided delta in large scale lacustrine: an example from Triassic Yanchang Formation in Ordos Basin. Earth Sci. Front. 20 (2), 19–28 (in Chinese).
Zhao, J.T., Tong, H.W., Yuan, J., et al., 2025. Three-dimensional strength and deformation characteristics of calcareous sand under various stress paths. Bull. Eng. Geol. Environ. 84 (1). https://doi.org/10.1007/s10064-025-04083-8.
Zheng, Y.H., Zhu, T.F., Chen, J.Q., et al., 2025. Relationship between pore-size distribution and 1D compressibility of different reconstituted clays based on fractal theory. Fractal and Fractional 9 (4), 235. https://doi.org/10.3390/fractalfract9040235.